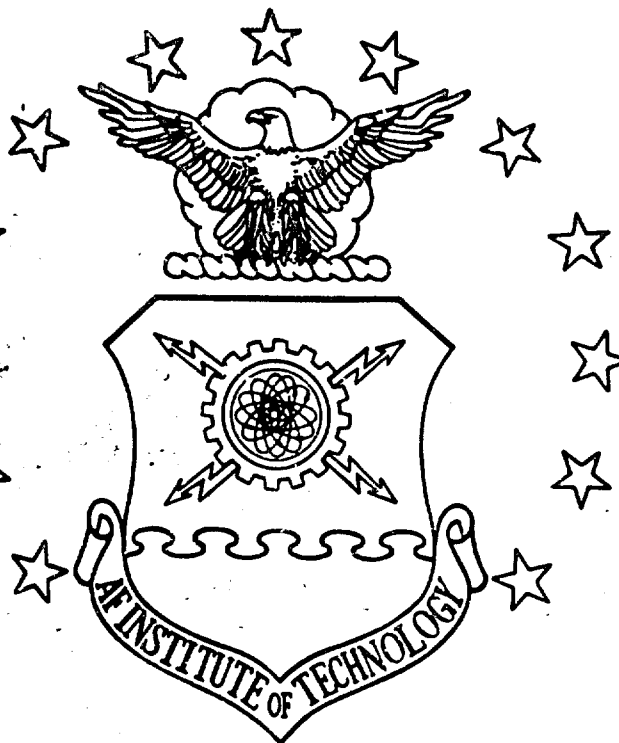


FILE COPY

Best Available Copy

1

AD-A206 023



COMPARISON OF SPLIT-FILM AND X-FILM  
MEASUREMENTS IN 2-D FLOW

THESIS

Timothy E. Fisk  
Captain, USAF

AFIT/GAE/AA/88D-16

DTIC  
ELECTE  
S D  
E

DEPARTMENT OF THE AIR FORCE

AIR UNIVERSITY

**AIR FORCE INSTITUTE OF TECHNOLOGY**

Wright-Patterson Air Force Base, Ohio

This document has been approved  
for public release and sales  
distribution is unlimited.

89 3 29 055

AFIT/GAE/AA/88D-16

COMPARISON OF SPLIT-FILM AND X-FILM

MEASUREMENTS IN 2-D FLOW

THESIS

Timothy E. Fisk  
Captain, USAF

AFIT/GAE/AA/88D-16

DTIC  
ELECTE  
S  
AE

AFIT/GAE/AA/88D-16

COMPARISON OF SPLIT-FILM AND X-FILM MEASUREMENTS IN 2-D FLOW

THESIS

Presented to the Faculty of the School of Engineering  
of the Air Force Institute of Technology

Air University

In Partial Fulfillment of the  
Requirements for the Degree of  
Master of Science in Aeronautical Engineering

Timothy E. Fisk, B.S.

Captain, USAF

November 1988

Approved for public release; distribution unlimited

## Table of Contents

Preface . . . . .	ii
List of Figures . . . . .	iii
List of Symbols . . . . .	v
Abstract . . . . .	viii
I. Introduction . . . . .	1
Purpose . . . . .	2
Background . . . . .	2
II. Experimental Procedure . . . . .	7
Data Collection . . . . .	7
Angle Calibration . . . . .	7
Velocity Calibration . . . . .	11
Tunnel Data Retrieval . . . . .	13
Accuracy . . . . .	16
III. Results and Discussion . . . . .	17
Empty Tunnel . . . . .	17
Cylinder . . . . .	20
IV. Conclusions and Recommendations . . . . .	24
Bibliography . . . . .	25
Appendix A: Calibration Relationships . . . . .	26
Appendix B: Fast Fourier Transforms . . . . .	31
Vita . . . . .	63

Accession For	
NTIS GRA&I	<input checked="" type="checkbox"/>
DTIC TAB	<input type="checkbox"/>
Unannounced	<input type="checkbox"/>
Justification	
By _____	
Distribution/	
Availability Codes	
Dist	Avail and/or Special
A-1	



## Preface

↳ The purpose of these experiments was to compare turbulence measurements using two types of velocity measurement probes: split-film and x-film. The goal is to determine the turbulent flow regimes where the split-film can be used to replace the x-film. → (to p. viii)

I thank my advisor LtCol Paul King for his guidance and patience through this effort, and his training in anemometry. Before the wind tunnel could be used for turbulence measurements, it required extensive restoration. I also thank Prof Hal Larsen for his effort in these renovations, and his zeal to educate me in the finer points of wind tunnel operation and aerodynamics. Mostly, thank-you Sharon for your extra effort running the household while I was off taking data.

Timothy E. Fisk

## List of Figures

Figure	Page
1. X-Film . . . . .	32
2. Split-Film . . . . .	33
3. Angle Calibrator . . . . .	34
4. Wind Tunnel Measurement . . . . .	35
5. Split-Film Angle Calibration . . . . .	36
6. X-Film Bisector Angle . . . . .	37
7. X-Film Angle Calibration . . . . .	38
8. Tunnel Velocity Calibration . . . . .	39
9. Split-Film Velocity Calibration . . . . .	40
10. X-Film Velocity Calibration . . . . .	41
11. Open Tunnel Data Retrieval . . . . .	42
12. Split-Film and X-Film $u'$ and $v'$ , Open Tunnel Centerline (VEL = 122 FT/SEC) . . . . .	43
13. Split-Film and X-Film FFT( $u'$ ) and FFT( $v'$ ), Open Tunnel Centerline (VEL = 122 FT/SEC) . . . . .	44
14. Cylinder Data Retrieval . . . . .	45
15. Split-Film and X-Film $u'$ and $v'$ , Behind Cylinder $X/D = 0.6$ , $Y/D = 0.0$ ( $Re = 144,000$ ) . . . . .	46
16. Split-Film and X-Film FFT( $u'$ ) and FFT( $v'$ ), Behind Cylinder $X/D = 0.6$ , $Y/D = 0.0$ ( $Re = 144,000$ ) . . . . .	47
17. Split-Film Turbulence, Open Tunnel . . . . .	48
18. X-Film Turbulence, Open Tunnel . . . . .	48
19. Split-Film vs X-Film Turbulence, Open Tunnel (VEL=97 FT/SEC)	50
20. Split-Film vs X-Film Turbulence, Open Tunnel (VEL=110 FT/SEC)	51

21. Split-Film vs X-Film Turbulence, Open Tunnel (VEL=122 FT/SEC)	52
22. Turbulence Scales, Open Tunnel (VEL=122 FT/SEC) . . . . .	53
23. Turbulence Intensity Behind Cylinder, u-Component (Re = 144,000) . . . . .	54
24. Turbulence Intensity Behind Cylinder, v-Component (Re = 144,000) . . . . .	55
25. Total Turbulence Intensity Behind Cylinder (Re = 144,000) . .	56
26. Velocity Behind Cylinder (Re = 144,000) . . . . .	57
27. Reynolds Shear Stress Behind Cylinder (Re = 144,000) . . . .	58
28. Turbulence Micro-scale Behind Cylinder, u-Component (Re = 144,000) . . . . .	59
29. Turbulence Micro-scale Behind Cylinder, v-Component (Re = 144,000) . . . . .	60
30. Turbulence Integral Scale Behind Cylinder, u-Component (Re = 144,000) . . . . .	61
31. Turbulence Integral Scale Behind Cylinder, v-Component (Re = 144,000) . . . . .	62
A-1. Split-Film Voltages Compared with Flow Angle . . . . .	30

## List of Symbols

a	King's law calibration constant
$A_1$	split-film velocity calibration constant
$A_2$	x-film velocity calibration constant
$A'$	split-film angle calibration constant
$A''$	x-film angle calibration constant
b	King's law calibration constant
$B_1$	split-film velocity calibration constant
$B_2$	x-film velocity calibration constant
$B'$	split-film angle calibration constant
$B''$	x-film angle calibration constant
$C_1$	split-film velocity calibration constant
$C_2$	x-film velocity calibration constant
d	cylinder diameter
$D_1$	difference of squared voltages, split film ( $E_1^2 - R_1^2 \cdot E_2^2$ )
$D_2$	difference of squared voltages, x-film
e	standard deviation of error
$E_1$	voltage, channel 1 (split or x-film)
$E_2$	voltage, channel 2 (split or x-film)
$E_{10}$	voltage, channel 1 with flow aligned with split (split-film) or bisector (x-film)
$E_{20}$	voltage, channel 2 with flow aligned with split (split-film) or bisector (x-film)
$E_{11}$	voltage, channel 1 with flow normal to film 1 (split-film)
$E_{21}$	voltage, channel 2 with flow normal to film 1 (split-film)
$E_{12}$	voltage, channel 1 with flow normal to film 2 (split-film)
$E_{22}$	voltage, channel 1 with flow normal to film 2 (split-film)



$E(n)$  spectral distribution function  
 $I_u$  integral scale, u-component  
 $I_v$  integral scale, v-component  
 $k$  kinetic energy of turbulence  
 $K_1$  split-film balance coefficient  
 $K_2$  x-film balance coefficient  
 $m_u$  micro-scale, u-component  
 $m_v$  micro-scale, v-component  
 $n$  frequency  
 $n_s$  sample rate  
 $R_s$  Reynolds shear stress  
 $Re_D$  Reynolds number based on diameter ( $U \cdot d / \text{viscosity}$ )  
 $S_1$  sum of the squared voltages, split-film ( $E_1^2 + K_1^2 \cdot E_2^2$ )  
 $S_2$  sum of the squared voltages, x-film  
 $St_n$  Strouhal number ( $n \cdot d / U$ )  
 $T_t$  total turbulence intensity  
 $T_u$  turbulence intensity, u-component  
 $T_v$  turbulence intensity, v-component  
 $T_w$  turbulence intensity, w-component  
 $u$  velocity component, axial (x) direction  
 $\bar{u}$  time average of  $u$   
 $u'$  fluctuation velocity component ( $u - \bar{u}$ )  
 $U$  total velocity (time dependent)  
 $v$  velocity component, radial (y) direction  
 $\bar{v}$  time average of  $v$   
 $v'$  fluctuation velocity component ( $v - \bar{v}$ )

$w'$  fluctuation velocity component in z-direction  
 $\alpha$  x-film wire angle from the bisector  
 $\theta$  flow angle with respect to the probe body  
 $\theta_x$  x-film bisector angle with respect to the probe body  
 $\theta_s$  split-film split location with respect to probe body

Abstract

(cont. from p. ii)  
 ↳

The split-film sensor is composed of two independent films supported by a quartz filament. The split-film's larger diameter makes it less sensitive to high frequency fluctuations than the x-film, but is able to measure higher flow angles than the x-film. The objective of this thesis is to compare turbulence measurements of the split-film with the more established x-film over a range of turbulence levels.

The results indicate problems using the split-film in regions of low velocity combined with low turbulence (Reynolds number based on film diameter less than 380 and turbulence intensity below 1.5<sup>70</sup> percent). The split-film provided better turbulence measurements than the x-film when used in regions of high turbulence (10 to 50 percent) with velocity fluctuations greater than 45 degrees from the mean.

The split-film is not capable of detecting flow reversals, but will give the proper direction of the velocity component normal to the split. This information is helpful because the magnitude of the Reynolds shear stress in reversing flow can still be determined using the split-film, but not the direction (sign).

*Results of split film measurements  
 at low frequency. These are*

## COMPARISON OF SPLIT-FILM AND X-FILM MEASUREMENTS IN 2-D FLOW

### I. Introduction

Currently 2-D turbulent flows are usually measured using x-film or x-wire sensors. X-film sensors (Figure 1) are chosen over x-wires when the testing environment might cause wire breakage. Both the x-film and x-wire provide excellent data in cases where the flow direction is known and the sensor can be aligned with the flow. If the flow varies over  $\pm 45$  degrees from the sensor's centerline, the x-configuration does not work. Also, the size of x-film and x-wire sensors detracts from their use in thin boundary layer flows due to the 2-D cross-section for these probes ranging up to 0.25 inches.

The split-film sensor (Figure 2), in use since 1970, is a recent innovation in anemometer sensing equipment. This sensor is composed of two electrically independent films supported by a single quartz fiber (TSI, TB 20, undated:1). The split-film is well suited for measuring 2-D turbulent flow (by design) due to its ability to measure velocity fluctuations up to  $\pm 90$  degrees from the mean flow direction. The split-film is capable of withstanding a more harsh environment than x-wires and x-films having film diameters less than 0.002 inches. The split-film's design also allows for use in thin boundary layers because its 2-D cross-section is equal to its diameter of 0.006 inches.

The split-film's larger diameter, however, contributes to the split-film having less sensitivity to velocity fluctuations than hot-wires and hot-films. Another problem associated with split-films stems

from internal heat transfer (cross-talk) from one film to the other through the quartz substrate (Ho, 1982:1240). This cross-talk was shown to cause inaccurate turbulence measurement at Reynolds numbers (based on film diameter) less than 24, and at low frequencies.

### Purpose

The purpose of these experiments is to compare turbulence measurements of the split-film with the more established x-film sensor over a range of turbulence levels and determine applications where the split-film gives accurate turbulence data. This information would be useful in situations where size limitations or large flow angles preclude the use of x-film sensors, and an alternative such as the split-film would be beneficial.

### Background

Anemometry. Hot-film anemometry is based on work done with hot-wires, where the flow velocity is related to the heat transfer in an electrically heated wire. The empirical law governing this heat transfer rate is known as King's law:

$$E^2 = a + b \cdot U_e^n \quad (1)$$

where  $E$  is the wire voltage;  $U_e$  is the flow velocity normal to the wire; and  $a$ ,  $b$ , and  $n$  are constants determined through calibration.

More recently, Siddall and Davies (1971:367) proposed a modification to King's law by applying a quadratic form to Equation (1) allowing for calibration constants which are easier to obtain:

$$E^2 = A + B \cdot U_e^{\frac{1}{2}} + C \cdot U_e \quad (2)$$

where A, B, and C are the new calibration constants.

These equations apply to a single sensor located in the flow. Measurement of velocity fluctuations in two directions requires dual sensors such as the split-film and x-film. Appendix A discusses the application of Equations (1) and (2) to x-film and split-film sensors.

Turbulence measurement. Measurement was accomplished in both low and high turbulence environments. Low turbulence was provided in an empty wind tunnel fitted with screens in order to provide turbulence levels below 2 percent at velocities ranging between 95 and 122 ft/sec. High turbulence was generated using the wake of a cylinder having a Reynolds number based on diameter of 144,000. Turbulence levels in the wake of a cylinder have been investigated by Townsend (1949), and by Uberoi and Freymuth (1969).

For Reynolds numbers greater than 300 the flow in the wake of the cylinder can be described in several stages. The developing stage consists of regular vortices up to 48 diameters downstream and continues until 400 diameters downstream of the cylinder; beyond 400 diameters, the flow becomes dynamically stable (Uberoi and Freymuth, 1969:1359). Uberoi and Freymuth (1969:1360) measured the turbulence for distances of 25, 50, 100, 200, 400, and 800 diameters downstream of a cylinder and the trends indicate the turbulence in the wake close to the cylinder (less than 25 diameters) could approach 50 percent for Reynolds numbers greater than 540. Due to size limitations in the 14 inch wind tunnel,

turbulence, in this thesis, was measured in the cylinder's wake within one diameter downstream of the cylinder.

The turbulence measurements used in these experiments to compare the x-film and split-film include such quantities as intensity, Reynolds shear stress, and scales.

Turbulence intensity is based on the mean of the squares of the fluctuating components of velocity. It is usually non-dimensionalized using the mean flow velocity. The turbulence intensity used for comparison was calculated from the following relationships (Cebeci and Smith, 1974:13,14):

$$T_u = (\overline{u'^2})^{1/2} / \bar{U} \quad (3)$$

$$T_v = (\overline{v'^2})^{1/2} / \bar{U} \quad (4)$$

$$T_w = (\overline{w'^2})^{1/2} / \bar{U} \quad (5)$$

$$T_t = [(\overline{u'^2} + \overline{v'^2} + \overline{w'^2})/3]^{1/2} / \bar{U} \quad (6)$$

where

$\bar{U}$  = time averaged value (mean) of total flow velocity

$T_u$  = turbulence component in the u-direction

$T_v$  = turbulence component in the v-direction

$T_w$  = turbulence component in the w-direction

$T_t$  = total turbulence intensity

$u'$  = u-component of the fluctuating velocity

$v'$  = v-component of the fluctuating velocity

$w'$  = velocity fluctuation component in the z-direction

If a 2-D assumption is used in these comparisons, with  $T_u \approx T_v \approx T_w$  (roughly), then  $T_w \approx T_t$ . Substituting this assumption into Equation (6) and solving gives:

$$T_t = [(T_u^2 + T_v^2)/2]^{\frac{1}{2}} \quad (7)$$

This gives the total turbulence ( $T_t$ ) as a function of the turbulence components  $T_u$  and  $T_v$ .

The level of turbulence is directly related to its kinetic energy, shown in the following relation (Cebeci and Smith, 1974:14):

$$k = \bar{U}^2 \cdot T_t^2 \quad (8)$$

where  $k$  is the kinetic energy of the turbulence per unit mass.

Another quantity important in the study of turbulence is the Reynolds shear stress, calculated using the product of the velocity fluctuations in two directions. Conservation of Reynolds shear stresses is used in the Reynolds stress transport equations-analogous to conservation of momentum in the Navier Stokes equations (Bradshaw, 1972:430). Reynolds shear stress ( $R_s$ ) is defined as:

$$R_s = -2 \cdot (\overline{u'v'}) / \bar{U}^2 \quad (9)$$

Turbulence scales may be divided into two types: the micro-scale, and the integral scale. These scales can be determined using Fourier transforms of the time traces of the fluctuating velocity components. Scales of turbulence are measures of the size of large-scale eddies or motion in the fluid (integral scale), and the smaller-scale disturbances being transported along with them (micro-scale) (Bradshaw, 1972:433). The integral scale ( $l$ ) was determined using the following method (Cebeci and Smith, 1974:21):



given  $I_u = \frac{1}{4} \cdot [\bar{U}/(\overline{u'^2})] \cdot \lim_{n \rightarrow 0} [E(n)]$  (10)

substituting  $\overline{u'^2} = [T_u \cdot \bar{U}]^2$  from Equation (3) (11)

and  $E(n) = \text{FFT}_u^2(n)$  from Appendix B (12)

gives  $I_u = \frac{1}{4} \cdot [1/(T_u^2 \cdot \bar{U})] \cdot \lim_{n \rightarrow 0} [\text{FFT}_u^2(n)]$  (13)

likewise  $I_v = \frac{1}{4} \cdot [1/(T_v^2 \cdot \bar{U})] \cdot \lim_{n \rightarrow 0} [\text{FFT}_v^2(n)]$  (14)

where  $n$  is the frequency;  $I_u$  and  $I_v$  are the integral scales in the  $u$  and  $v$  directions, respectively;  $\text{FFT}_u$  and  $\text{FFT}_v$  are the Fast Fourier transforms (Appendix B) of  $u'$  and  $v'$  velocity components; and  $E(n)$  is the spectral distribution function.

The micro-scale ( $m$ ) was determined using the following method (Cebeci and Smith, 1974:22):

$$1 / m_u = 2 \cdot [\pi^2 / (\bar{U}^2 \cdot \overline{u'^2})] \cdot \sum_{n=0}^{\infty} [n^2 \cdot E(n)] \quad (15)$$

and substituting Equations (11) and (12) yields

$$1 / m_u^2 = 2 \cdot [\pi / (\bar{U}^2 \cdot T_u)]^2 \cdot \sum_{n=0}^{\infty} [n^2 \cdot \text{FFT}_u^2(n)] \quad (16)$$

likewise  $1 / m_v^2 = 2 \cdot [\pi / (\bar{U}^2 \cdot T_v)]^2 \cdot \sum_{n=0}^{\infty} [n^2 \cdot \text{FFT}_v^2(n)]$  (17)

where  $m_u$  and  $m_v$  are the micro-scales in the  $u$  and  $v$  directions.

## II. Experimental Procedure

### Data collection

The sensors compared in these experiments were both manufactured by Thermal Systems Inc. (TSI). The split-film, model 1288 (Figure 2); and the x-film, model 1241-10 (Figure 1); were operated using TSI's IFA-100 Flow Analyzer (transducer). This transducer includes two TSI model 150 Anemometers each supported by a model 157 Signal Conditioner. The signal conditioners provide an adjustable low-pass filter ranging from 1 Hz to 500 KHz. Output bridge voltages from each anemometer, after passing through the signal conditioner, were converted to digital information using a Qua-tech analog-to-digital (A/D) converter installed in a Zenith Z-248 personal computer. This A/D system provided 4 channel simultaneous sampling (only 2 channels were used) for frequencies ranging from 160 Hz to 32 KHz. The digital information imported to the computer via the A/D converter was then converted to voltage data for each channel using software written in Microsoft (c) Basic. All calibration and comparison data retrieval for both probes was accomplished using the same TSI dual channel 18 inch probe support and connecting cables.

### Angle calibration

Each sensor provided by TSI includes a recommended operating resistance for each channel which gives an operating temperature of 250 degrees C. Both channels on the transducer were set according to TSI's recommendations prior to angle calibration.

The frequency response of both channels on each sensor was tested using a square wave generator provided with the anemometer. The bridge output for each channel was observed with an oscilloscope and the frequency compensation was adjusted on each bridge until the frequency response of both channels matched. This procedure was accomplished prior to calibration and data collection in order to assure balanced frequency response for each sensor.

Appendix A gives details on the relationships used for angle calibration and shows that the angle calibration procedures used for both sensors did not require the flow velocity be known. The sensors were calibrated using a rotation mechanism mounted to an air chamber (Figure 3). Calibration data was obtained for each sensor using a range of angles and three velocities for each angle. The velocities used were approximately 63, 90, and 125 ft/sec; chosen to be in the range of velocities used later for tunnel data comparisons.

Split-film. In order for the split-film to function properly, both halves of the film must operate at the same temperature, defined as "balance". The recommended operating resistances for each channel of the split-film are not accurate enough to balance the sensor, and further adjustment is required. The procedure outlined by TSI used to balance the sensor also gives the angular location of the split relative to the probe (sensor) body ( $\theta_s$ ) (TSI, TB 20, undated:7-9). This procedure relies on the following relationships:

$$R_1 = E_{10}/E_{20} \quad (18)$$

$$K_1 = [(E_{12} \cdot E_{11}) / (E_{21} \cdot E_{22})]^{1/2} \quad (19)$$

where

- $K_1$  = balance factor, independent of flow velocity
- $E_{10}$  = voltage, channel 1 with flow aligned with split
- $E_{20}$  = voltage, channel 2 with flow aligned with split
- $E_{11}$  = voltage, channel 1 with flow normal to film 1
- $E_{21}$  = voltage, channel 2 with flow normal to film 1
- $E_{12}$  = voltage, channel 1 with flow normal to film 2
- $E_{22}$  = voltage, channel 2 with flow normal to film 2

An iterative procedure is used to balance the probe and obtain  $\theta_s$  by using above Equations (18) and (19) and the angle calibrator along with minor adjustments to the operating resistance of one channel. The angle  $\theta_s$  is described by the flow angle which provides the same value for  $K_1$  in both Equations (18) and (19) while allowing for  $K_1$  to remain constant over a range of air velocities.

After  $K_1$  and  $\theta_s$  were found for the split-film, the probe was calibrated using the following relationships described by TSI (TSI, TB 20, undated:2) as modified in Appendix A:

$$D_1 / \sin(\theta + \theta_s) = A' \cdot S_1^{B'} \quad (20)$$

$$\text{defining:} \quad D_1 = E_1^2 - K_1^2 \cdot E_2^2 \quad (21)$$

$$S_1 = E_1^2 + K_1^2 \cdot E_2^2 \quad (22)$$

where

- $E_1$  = voltage, channel 1
- $E_2$  = voltage, channel 2
- $\theta$  = flow angle with respect to probe body
- $\theta_s$  = angle between split and probe body
- $S_1$  = sum of squared voltages, corrected by  $K_1$  (definition)

$D_1$  = Difference of squared voltages, corrected by  $K_1$  (definition)  
 $A'$  and  $B'$  = calibration constants, independent of temperature

Angle calibration data was obtained using the calibrator, shown in Figure 3, by positioning the probe body at a range of angles with respect to the flow and measuring the voltage for each channel (three velocities and ten angles were used). Least-squares curve fitting was used to calculate the constants  $A'$  and  $B'$  with results shown in Figure 5.

X-film. The angle between the probe body and the bisector of the two films was measured using a reversed bench microscope. The image of the "X" was projected and traced at 180 degrees and 0 degrees axial probe body rotation as illustrated in Figure 6. The angle between the two bisectors gives two times the angle between the probe body and "X" bisector ( $\theta_x$ , the bisector angle). Once  $\theta_x$  was known, the probe was positioned in the angle calibrator such that the bisector was lined up with the air flow. The operating resistance of one channel was adjusted until both channels gave the same voltage level within the accuracy of measurement equipment used (oscilloscope or voltmeter). The ratio of the voltages for each channel ( $K_2$ , approximately equal to one) was then calculated:

$$K_2 = E_{10}/E_{20} \quad (23)$$

where

$E_{10}$  = voltage, channel 1 with flow aligned with the bisector  
 $E_{20}$  = voltage, channel 2 with flow aligned with the bisector  
 $K_2$  = balance factor, independent of flow velocity

Once  $\theta_x$  and  $K_2$  were known, the probe was calibrated for angle measurement in the same manner as the split-film using the following relationships developed in Appendix A:

$$D_2 / \tan(\theta + \theta_x) = A'' \cdot S_2^{B''} \quad (24)$$

defining:  $D_2 = E_1^2 - K_2^2 \cdot E_2^2 \quad (25)$

$$S_2 = E_1^2 + K_2^2 \cdot E_2^2 \quad (26)$$

where

$E_1$  = voltage, channel 1

$E_2$  = voltage, channel 2

$\theta$  = flow angle with respect to probe body

$\theta_x$  = angle between bisector and probe body

$S_2$  = sum of squared voltages, corrected with  $K_2$  (definition)

$D_2$  = difference of squared voltages, corrected with  $K_2$  (definition)

$A''$  and  $B''$  = calibration constants, independent of temperature

The procedure for obtaining x-film angle calibration constants is identical to the split-film and the results are shown in Figure 7.

### Velocity calibration

The probes were calibrated for velocity in the 14 inch tunnel (discussed later) prior to taking turbulence measurements in order to reduce errors caused by temperature changes and to avoid using temperature correction factors sometimes used in velocity calibration. Before the tunnel could be used for velocity calibration, it was calibrated using a pitot-static tube. The pitot-static tube was placed in the tunnel as shown in Figure 4 and static and total pressure readings were taken. These readings were compared with the static pressure at locations 1 and 2 along the tunnel wall for a range of velocities, with

the results shown in Figure 8. Bernouli's equation, based on incompressible flow, was used to convert the pressures to velocity.

Split-film. The split-film was positioned at the tunnel centerline and voltage measurements taken for velocities ranging from 50 to 140 ft/sec; chosen to be in the range of velocities used for tunnel data comparisons. The probe was calibrated for velocity measurement using the following relationship given by TSI (TSI, TB 20, undated:2) as described in Appendix A:

$$S_1 = A_1 + B_1 \cdot U^{\frac{1}{2}} + C_1 \cdot U \quad (27)$$

where  $U$  is the tunnel velocity; and  $A_1$ ,  $B_1$ , and  $C_1$  are constants. Least-squares was used to calculate the velocity calibration constants and the results for one temperature are shown in Figure 9.

X-film. The x-film procedure is similar to the split-film except it was necessary to determine the flow angle ( $\theta$ ) first using Equation (24), the predetermined constants  $A''$  and  $B''$ , and the angle correction factor  $\theta_x$ .

The relation used to obtain the x-film velocity constants is (Appendix A):

$$S_2 = A_2 + B_2 \cdot [U \cdot \cos(\theta + \theta_x)]^{\frac{1}{2}} + C_2 \cdot U \cdot \cos(\theta + \theta_x) \quad (28)$$

where  $A_2$ ,  $B_2$ , and  $C_2$  are constants valid for all flow angles. Least-squares was again used to calculate the velocity calibration constants and the results for one temperature are shown in Figure 10.

### Tunnel data retrieval

Velocity and turbulence was measured in a 14 inch diameter subsonic wind tunnel. This tunnel was a recirculating type with an air exchanger upstream of the compressor designed to maintain a constant air temperature in the tunnel. Screens (2) were fitted upstream of the test section to reduce the turbulence generated by the compressor and the turning vanes (located in the corners of the tunnel). The test section included a model support yoke mounted in the bottom and a probe positioning mechanism mounted to the top. The probe positioning mechanism was designed to provide symmetric probe blockage in the tunnel by aligning the probe support with the flow using a rod traversing through both the top and bottom of the tunnel (Figure 4). Measurements were accomplished in the empty tunnel (except for model support yoke) for low turbulence, and behind a three inch diameter cylinder mounted to the model support yoke for high turbulence.

Empty tunnel. Each probe was positioned in the same x (axial) location and data was obtained by traversing in the y (radial) direction. Figure 11 shows the coordinate system used and the locations chosen. Three velocities were sampled at each data location: 97, 110, and 122 feet/sec. These velocities were chosen in order to remain in the range of incompressible flow assumptions, and to be consistent with the flow velocity used for the three inch cylinder (high turbulence) comparisons.

The signal conditioner's low-pass filter for each channel was set for a cut-off frequency of 8 KHz, and 512 voltages were sampled from each channel simultaneously at 16 KHz for each data location and



velocity. Fast Fourier transform (FFT) analysis (Appendix B) of the voltage data was used to determine the frequency response of the probes, and previous test runs showed higher sampling rates did not yield significant information at higher frequencies. The sample rate was chosen to be twice that of the filter to reduce aliasing (anti-alias filtering). Instantaneous velocity components were calculated from the inverse of Equations (20) and (27) for the split-film, or (18) and (24) for the x-film. For the split-film, the flow angle was calculated from:

$$\theta = \text{ARCSIN}[D_1 / (A_1 \cdot S_1^{B_1})] - \theta_a \quad (29)$$

and the velocity calculated by completing the square in Equation (27):

$$M = B_1^2 + 4 \cdot C_1 \cdot (S_1 - A_1) \quad (30)$$

$$U = [(M^{1/2} - B_1) / (2 \cdot C_1)]^2 \quad (31)$$

Knowing the instantaneous velocity (U) and direction ( $\theta$ ), the velocity components are found by:

$$u = U \cdot \cos(\theta) \quad (32)$$

$$v = U \cdot \sin(\theta) \quad (33)$$

where u and v are typical of the instantaneous velocity components in the x and y direction. The same procedure may be applied to x-film Equations (24) and (28).

Figure 12 shows representative fluctuation velocity traces for the split and x-film where:

$$u' = u - \bar{u} \quad (34)$$

$$v' = v - \bar{v} \quad (35)$$

where  $u'$  and  $v'$  are the fluctuating velocities; and  $\bar{u}$  and  $\bar{v}$  are the time-averaged (mean) values of  $u$  and  $v$ .

Figure 13 shows the Fast Fourier transforms (FFT's) of the  $u'$  and  $v'$  traces given in Figure 12. The magnitude of the FFT's (ft/sec) shown in Figure 13 can best be described by the square root of the energy contained for each frequency.

Cylinder. Figure 14 shows the locations where cylinder data was obtained for the two probes. A flow velocity of 92.3 ft/sec was used to give a Reynolds number based on diameter ( $Re_D$ ) of 144,000. This Reynolds number was used to determine the Strouhal number ( $St$ ) for the Kármán vortex street behind the cylinder (Schlichting, 1979:31,32). The frequency of the vortex was then estimated:

$$n = U \cdot St / d \quad (36)$$

where  $n$  is the frequency,  $U$  the flow velocity (92.3 ft/sec),  $d$  the cylinder diameter (3 inches), and  $St$  the Strouhal number ( $\approx 0.19$ ) based on Schlichting's Figure 2.9 for  $Re_D = 144,000$  (Schlichting, 1979:32).

This gave the frequency,  $n \approx 70$  Hz for the vortex shedding behind the cylinder. This information was used to choose the sampling rate and filter used for data acquisition behind the cylinder. The anemometer's signal conditioner was set for a cut-off frequency of 4 KHz, and 512 voltages were sampled from each channel simultaneously at 8 KHz for each data location.

This choice allows approximately 4.5 cycles of the shedding vortices for the FFT to sample; calculated by:

$$\text{cycles} = N \cdot n / n_s \quad (37)$$

where  $N$  is the number of sample data points (512),  $n$  is the frequency of the vortices (70 Hz), and  $n_s$  is the sample rate (8000 Hz).

Figure 15 shows representative  $u'$  and  $v'$  traces behind the cylinder and Figure 16 shows the FFT's of these velocities. The frequencies of the FFT's in Figure 16 were only plotted up to 800 Hz in order to highlight the behavior of the fluctuations at the low frequencies.

#### Accuracy

Voltage measurements taken using the computer were within  $\pm 0.002$  volts due to analog to digital conversion accuracy; pressure measurements using the micro-manometer were within  $\pm 0.005$  inches  $H_2O$ ; and probe locational measurements were within  $\pm .005$  inches due to machining tolerances of the probe positioning mechanism (excluding probe size differences). The wind tunnel maintained mean velocity within  $\pm 2$  ft/sec. Turbulence measurements in the open tunnel were repeatable within 10 percent error.

### III. Results and Discussion

The values used to compare turbulence measurements made with the x-film and split film were turbulence intensity, Reynolds shear stress, integral scale, and micro-scale. The relationships used to calculate these values are outlined in Chapter I. Turbulence intensities ( $T_u$ ,  $T_v$ , and  $T_t$ ) were determined using Equations (3), (4), and (7); Reynolds shear stresses ( $R_s$ ) using Equation (9); integral scales ( $I_u$  and  $I_v$ ) using Equations (13) and (14); and micro-scales ( $m_u$  and  $m_v$ ) using Equations (16) and (17). The value of the FFT as  $n \rightarrow 0$  used to calculate the integral scale in Equations (13) and (14) was estimated by averaging the first 3 frequency data points (Figures 13 and 15).

#### Empty tunnel

Figure 17 shows turbulence results using the split-film for three velocities in the empty tunnel. Figure 18 shows this information using the x-film. Figures 19-21 compare the turbulence levels obtained using the two probes along with the Reynolds stresses for each velocity. The information shows turbulence levels ranging from 0.3 percent up to 2.6 percent.

Both probes indicate lower turbulence in the bottom of the tunnel (0.3 - 1.25 percent) than in the top (1.0 - 2.6 percent). This was most likely due to the model support yoke remaining in the tunnel's lower half (Figure 4). This obstruction effectively forced the air to flow toward the top of the tunnel, creating higher turbulence. Both probes indicated this flow vectoring effect with measured flow deflection

angles of up to two degrees from the tunnel centerline and slightly higher velocities at the top of the tunnel (no figure).

Turbulence components  $T_u$  and  $T_v$  for both probes showed a more isotropic ( $T_u \approx T_v$ ) nature as the velocity increased (Figures 17 and 18). Figure 17 shows  $T_u$  was larger than  $T_v$  for most cases using the split-film; however, Figure 18 shows the opposite trend for the x-film. Further examination of Figures 19-21 indicates the v-components of turbulence generally agree, with the x-film showing slightly higher levels in the higher turbulence region of the tunnel ( $Y \geq 0$ ).

The major discrepancy involves the u-component of turbulence. Especially at lower levels they did not agree, with  $T_u$  for the split-film being larger than the x-film. In fact,  $T_u$  for the split-film did not go below one percent. In order to help resolve this deviation, a single-film (hot-film) probe was used to measure the total turbulence in the region of the highest discrepancy (tunnel location  $Y = -3.0$  inches) at 122 ft/sec tunnel velocity. The turbulence obtained using the single-film at this location agreed with the x-film as shown by the point labeled "hot-film" in Figure 21.

Assuming the x-film data in this case to be accurate based on the single-film data, an explanation for the split-film indicating higher turbulence than present in the flow is needed. The u component of velocity is measured using the sum of the voltages of the top and bottom halves of the split-film's cylinder, while the difference of the voltages effectively gives the v-component as described by Equations (29) and (31). In order for  $T_u$  to measure higher than actual, the instantaneous voltages for each film (heat transfer) must sum together

such that the RMS value ( $T_u$ ) of this sum becomes higher than expected. The RMS value of the instantaneous difference in voltages ( $T_v$ ), as mentioned earlier, generally agreed with  $T_v$  for the x-film.

One possibility for  $T_u$  to be high could be due to thermal cross-talk between the films. Ho demonstrated significant thermal cross-talk, or internal heat transfer, for the same model split-film used in these experiments at film Reynolds numbers (based on diameter) less than 24 for low level turbulence (electrically induced) (Ho, 1982:1240). The Reynolds number in this thesis ranged from 300 (95 feet/sec) to 380 (122 feet/sec) for the split-film. The convection heat transfer rate (Nusselt number) for these Reynolds numbers is about four times larger than Ho's experiments (Holman, 1978:217). Eventually, as the Reynolds number is increased, the convection heat transfer should become much larger than the internal conduction and the error in measuring  $T_u$  should become tolerable. In order to verify decreased error with increased Reynolds numbers, the split film was placed in higher velocity flows at  $Y = -3$  inches. At 186 feet/sec, or a Reynolds number of 584,  $T_u$  and  $T_v$  became nearly the same at 0.77 and 0.85 percent, respectively.

For the higher turbulence levels, the split-film and x-film were in better agreement. Ho's experiments showed the effects of cross-talk were diminished when electrically input fluctuations simulated turbulence levels greater than four percent at a Reynolds number of 14.4 (Ho, 1982:Figure 7, 1243). This can be compared with results from Figures 18-21 where the split-film did not appear to give accurate readings in turbulence below 1.5 percent in Reynolds numbers below 380.

Another possible stabilizing effect of higher turbulence levels on the split-film could be due to increased heat transfer area on each side of the split film from fluctuations in the flow angle causing the flow separation point on the cylinder to change. Large fluctuations could effectively cause higher heat transfer rates to both halves of the split-film due to increased area. Conversely, low turbulence combined with low velocity could effectively create unbalanced heat transfer.

Reynolds shear stress values shown in Figures 19-21 for both probes were of the same order, ranging from  $-0.0002$  to  $0.0002$ ; however, the values for the probes did not generally agree. Integral and micro-scales were compared in Figure 22 for one velocity (122 feet/sec). The micro-scales for both components ranged from 0.030 to 0.032 inches and agreed within 2.5 percent between probes. The integral scales ranged from 1.8 to 13 inches for the u-component and 1.8 to 38.7 inches for the v-component. The integral scales for the two probes agreed well when the turbulence levels measured the same.

Another effect which could have caused errors for both probes could be due to using static calibration data to predict turbulence. More accurate turbulence measurement would be possible if the probe could be calibrated in a flow of known turbulence.

### Cylinder

Figures 23-25 illustrate turbulence levels in the flow behind a cylinder measured with the split-film and x-film. The results show good agreement with the 50 percent level expected for the wake as discussed in Chapter I (page 3). The u-component of turbulence (Figure 23) shows fair agreement for most data locations; while the v-component (Figure

24) is much different between the two probes. A single-film (hot-film) probe was again used to determine the discrepancy in the turbulence measurements; and Figure 25 shows the total turbulence levels of all three probes. The results show the split-film gives higher turbulence levels in the wake behind the cylinder than the x-film and hot-film, with the x-film giving the lowest readings. In this situation the split-film is most likely giving better turbulence information than either the x-film or hot film due to geometry limitations of the latter two probes. This is discussed in more detail below.

The x-film is limited to flow angles within  $\pm 45$  degrees (typically) of the probe body (Figure 8). If the flow exceeds this limitation, the probe will react as though the flow angle is less than  $\pm 45$  degrees. For example, the probe would react to a 40 degree flow angle with approximately the same voltage readings as a 50 degree angle (excluding blockage). In the high turbulence area behind the cylinder at  $X/D = 0.6$ , the fluctuating velocities  $u'$  and  $v'$  shown in Figure 15 to range from -40 to 40 ft/sec are nearly the same magnitude as the mean flow velocity at this location of 40 ft/sec as shown in Figure 26. In this situation the x-film would not be capable of accurately measuring these fluctuations and would damp-out any fluctuations at angles greater than 45 degrees.

Another geometry problem of the x-film and hot-film could be caused by flow reversals behind the cylinder. Both probes could contribute substantially higher self-blockage to reverse flow than the split film. The split-film has a small diameter rod, as shown in Figure 2, supporting the sensor and should be less affected by reverse flow.



Figure 26 shows the average velocity behind the cylinder measured with the split-film and x-film probes; and the values show good agreement. As discussed earlier, flow reversals most likely exist behind the cylinder at this Reynolds number-as shown in Schlichting's Figure 2.6 (Schlichting, 1979:10). While the x-film is not capable of determining flow directions exceeding  $\pm 45$  degrees, the split-film (Figure 1), as used in these measurements, will always give the proper direction of velocity in the  $v$  direction. If the split-film is exposed to flow velocities greater than  $\pm 90$  degrees, the direction of  $u$  becomes unknown. Direction arrows in Figure 26 show this uncertainty.

The Reynolds shear stresses, shown in Figure 27, agreed at locations where x-film and split-film turbulence measured the same. Where disagreement occurs as shown in Figure 27 (for example  $X/D = 0.4$  and  $Y/D = 0.6$ ), the disagreement is most likely due to the same x-film limitation for fluctuations greater than  $\pm 45$  degrees as discussed earlier concerning turbulence measurement.

The micro-scales in the  $u$  and  $v$  directions ranged from 0.067 inches at  $Y/D = 0.8$  to 0.012 inches in the center of the wake, and compared well for both probes at all axial ( $X/D$ ) locations (Figures 28 and 29). The integral scales in the wake of the cylinder ( $Y/D \leq 0.5$ ) shown in Figures 30 and 31 gave similar information for the x-film and split-film. In this location, the scales ranged from one to five inches for both components: this was most likely due to the influence of the three inch cylinder diameter. The integral scale values approached those obtained in the open tunnel (Figure 22) when the probes were above the

cylinder's influence. The values of the integral scale at  $X/D = 0.0$  are not shown due to inconsistencies in measurement for both probes.

Finally, the Strouhal number ( $St$ ) correlation described by Equation (36), where the vortex shedding frequency was predicted to be 70 Hz behind the cylinder, was compared with the FFT's of both probes shown in Figure 16. The  $u'$  FFT's for the split-film and x-film show peak values at 40 and 70 Hz while the  $v'$  components showed peak values at 30 and 110 Hz for both probes. The differences between the predicted 70 Hz and the measured  $u'$  and  $v'$  values could be due to the frequency measurement increment of 16 Hz being too large to give accurate readings. Another possibility could be the frequencies shown in Figure 16 are harmonics of the actual shedding frequency.

Also, in all of the above tests, nowhere did it appear that film diameter affected the differences in the x-film and split-film probes other than the obvious higher frequency response of the smaller diameter films of the x-film.

#### IV. Conclusions and Recommendations

The results show split-film turbulence measurements in regions of low velocity combined with low turbulence (Reynolds number, based on the split-film diameter, below 380 and turbulence below 1.5 percent) do not compare well with the x-film. For this low turbulence (below 1.5 percent), the split-film indicates higher levels of turbulence than the x-film and this was explained to be most likely due to internal conduction heat transfer in the split-film. Further study in this area, using flows with a known turbulence level would be helpful.

The split-film showed an advantage over the x-film when used in regions of high turbulence (10 to 50 percent) with velocity fluctuations greater than 45 degrees from the mean. The split-film is not capable of detecting flow reversals, but will only give the proper direction of the velocity component normal to the split. Thus, the split-film can be used to determine the magnitude of the Reynolds shear stress, but not the direction (sign).

Scales of turbulence measured about the same for both probes, especially when the measured turbulence levels agreed.

## Bibliography

Bradshaw, P. "The Understanding and Prediction of Turbulent Flow," Aeronautical Journal: 403-406 (July 1972)

Cebeci, Tuncer and Smith, A. M. O. Analysis of Turbulent Boundary Layers. Florida: Academic Press, Inc., 1974.

Ho, Chih-Ming. "Response of a Split Film Probe Under Electrical Perturbations," Review of Scientific Instrumentation, 53(8): 1240-1245 (August 1982).

Holman, J. P. Heat Transfer. New York: McGraw-Hill Book Company, 1976.

Press, William H. and others. Numerical Recipes: The Art of Scientific Computing. Cambridge University Press, 1986.

Schlichting, Hermann. Boundary-Layer Theory. New York: McGraw-Hill Book Company, 1979.

Siddall, R. G. and Davies, T. W. "An Improved Response Equation for Hot-Wire Anemometry," Intl Journal of Heat and Mass Transfer, 15: 367-368 (1972).

----- Technical Bulletin TB 20 TSI Split Film Sensor Calibration and Application. Thermal Systems Incorporated, 500 Cardigan Road, St Paul MN.

Uberoi, Mahinder S. and Freymuth, Peter. "Spectra of Turbulence in Wakes behind Circular Cylinders," The Physics of Fluids, 12(7): 1359-1363 (July 1969).

## Appendix A. Calibration Relationships

### Split-film

The following relationships were used to calibrate the split-film sensor. The relationship for velocity calibration given by the manufacturer (TSI) is (TSI, TB 20, undated:2):

$$E_1^2 + K_1^2 \cdot E_2^2 = F_1(U) \quad (A.1)$$

where

$E_1$  = voltage, channel 1

$E_2$  = voltage, channel 2

$K_1 = E_{10}/E_{20}$  when flow is directed at the split, Equation (18)

$F_1(U)$  = function of the flow velocity (U), independent of flow angle

Equation (A.1) is based on the assumption that  $F_1(U)$  is independent of the flow angle. To verify this assumption, the sum of the squared voltages defined by Equation (22) was measured through a range of angles and velocities and plotted in Figure A-1.  $F_1(U)$  may be represented by King's law as shown by Equation (1) or a quadratic approach as shown by Equation (2) (Siddall and Davies, 1971:367).

To calibrate for the flow angle, TSI offers this relationship (TSI, TB 20, undated:2):

$$E_1^2 - K_1^2 \cdot E_2^2 = F_2(U) \cdot \sin(\theta) \quad (A.2)$$

where  $\theta$  is the angle between the plane of the split and the flow, and  $F_2(U)$  is also independent of angle.

Since  $F_2(U)$  and  $F_1(U)$  are only functions of velocity,  $F_2(U)$  is related to the sum of the squared voltages ( $S_1$ ).

Therefore, Equation (A.2) can be written in the form:

$$E_1^2 - K_1^2 \cdot E_2^2 = F(S_1) \cdot \sin(\theta) \quad (A.3)$$

where  $F(S_1)$  is a function of the squared voltages. The calibration relationship becomes:

$$D_1 / \sin(\theta) = A' \cdot S_1^{B'} \quad (A.4)$$

where  $A'$  and  $B'$  are constants and  $D_1 = E_1^2 - K_1^2 \cdot E_2^2$

This gives an angle calibration relationship using only the voltages from the split film without knowing the actual air velocity. An example of the results obtained using these relationships is shown in Figures 5 and 9.

#### X-film

Given the x-film geometry shown in Figure 2, and King's law for each film of the x-film:

$$E_1^2 = G_1(U) \cdot \cos(\theta - \alpha) \quad (A.5)$$

$$E_2^2 = G_2(U) \cdot \cos(\theta + \alpha) \quad (A.6)$$

where  $G_1(U)$  and  $G_2(U)$  are independent of flow angle,  $\theta$  is the flow angle with respect to the x-film bisector, and  $\alpha$  is the angle between the x-bisector and the normal component of each film (Figure 6).

If the temperature (operating resistance) of each film is adjusted so that the anemometer bridge voltages for each film (channel) are nearly equal when the flow is directed at the bisector of the x-film ( $\theta = 0$ ),  $G_1(U)$  and  $G_2(U)$  become nearly equal. Using these relationships, adding Equations (A.5) and (A.6), and simplifying:

$$S_2 = \cos(\theta) \cdot \sin(\alpha) \cdot [G_1(U) + G_2(U)] + \cos(\alpha) \cdot \sin(\theta) \cdot [G_1(U) - G_2(U)] \quad (A.7)$$

where  $S_2 = E_2^2 + K_2^2 E_2^2$ ; and  $K_2 = E_1/E_2$  when the flow is directed at the bisector ( $K_2 \approx 1$ ). Further reduction of Equation (A.7) yields:

$$S_2 = G(U) \cdot \cos(\theta) \cdot \sin(\alpha) \quad (A.8)$$

where  $G(U) = G_1(U) + G_2(U)$  and  $G_1(U) - G_2(U) \approx 0$

This relationship (A.8) may be used to calibrate for velocity and the term  $\sin(\alpha)$  can be included in the calibration constants.

To calibrate the x-film for the flow angle, the difference of the squared voltages is used. Subtracting Equation (A.6) from (A.5) and using the same assumptions used to derive Equation (A.8) gives the following:

$$D_2 = F(U) \cdot \sin(\theta) \cdot \cos(\alpha) \quad (A.9)$$

where  $D_2 = E_2^2 - K_2^2 E_2^2$

Dividing Equation (A.9) by (A.8) gives:

$$D_2 / \tan(\theta) = A'' \cdot S_2^{B''} \quad (A.10)$$

where  $A''$  and  $B''$  are calibration constants which include  $\alpha$ .

This gives an angle calibration relationship using only the voltages from the x-film, without knowing the actual air velocity. An example of the results is shown in Figures 7 and 10.



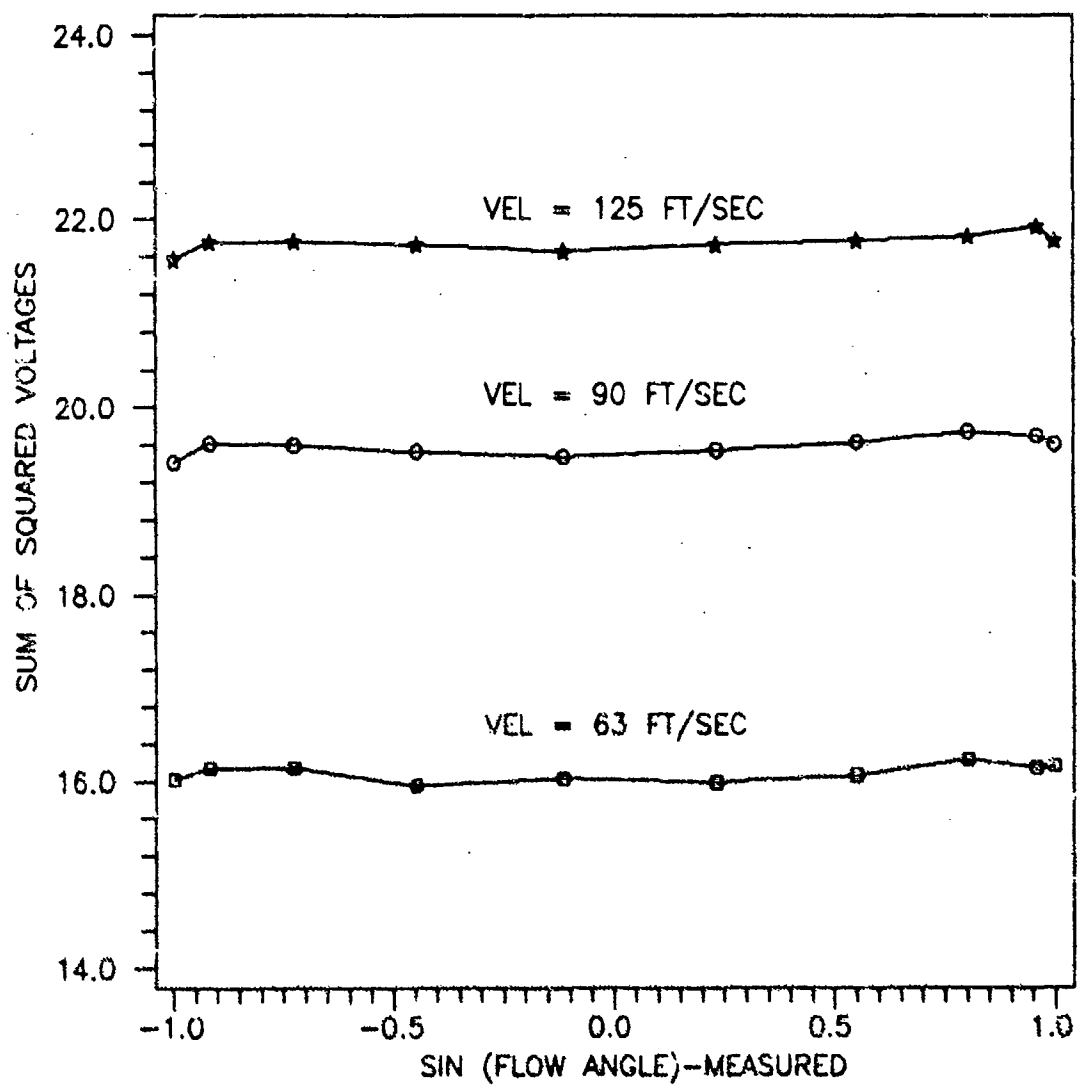


Figure A-1. Split-Film Voltages Compared with Flow Angle

## Appendix B. Fast Fourier Transforms

Fast Fourier transforms (FFT's) were used to examine the energy content of the velocity traces. For example, the spectral distribution function for the instantaneous velocity fluctuations ( $E_1$ ) given by (Cebeci and Smith, 1974:20):

$$\overline{u'(t)^2} = \int_0^{\infty} E(n) \, dn = \sum_{n=0}^{\infty} E(n) \quad (B.1)$$

where  $u'$  is the fluctuating velocity in the time domain,  $n$  is the frequency, and  $E(n)$  is the spectral distribution function.

Using Parseval's theorem:

$$\overline{u'(t)^2} = \frac{1}{N} \cdot \sum_{k=1}^N u'_k(t) = \frac{1}{N^2} \cdot \sum_{k=1}^N F_k^2(n) \quad (B.2)$$

where  $F(n)$  is the discrete Fourier transform of  $u'(t)$ ,  $k$  is the sample data point, and  $N$  is the number of samples. Therefore,

$$(1/N^2) \cdot F_k^2(n) = E(n) \quad (B.3)$$

The discrete fourier transform used to find  $F(n)$  was the Fast Fourier Transform (FFT) method (Press, and others, 1986:390-395) where the FFT is defined as:

$$FFT_U^2(n) = (1/N^2) \cdot F_k^2(n) = E(n) \quad (B.4)$$

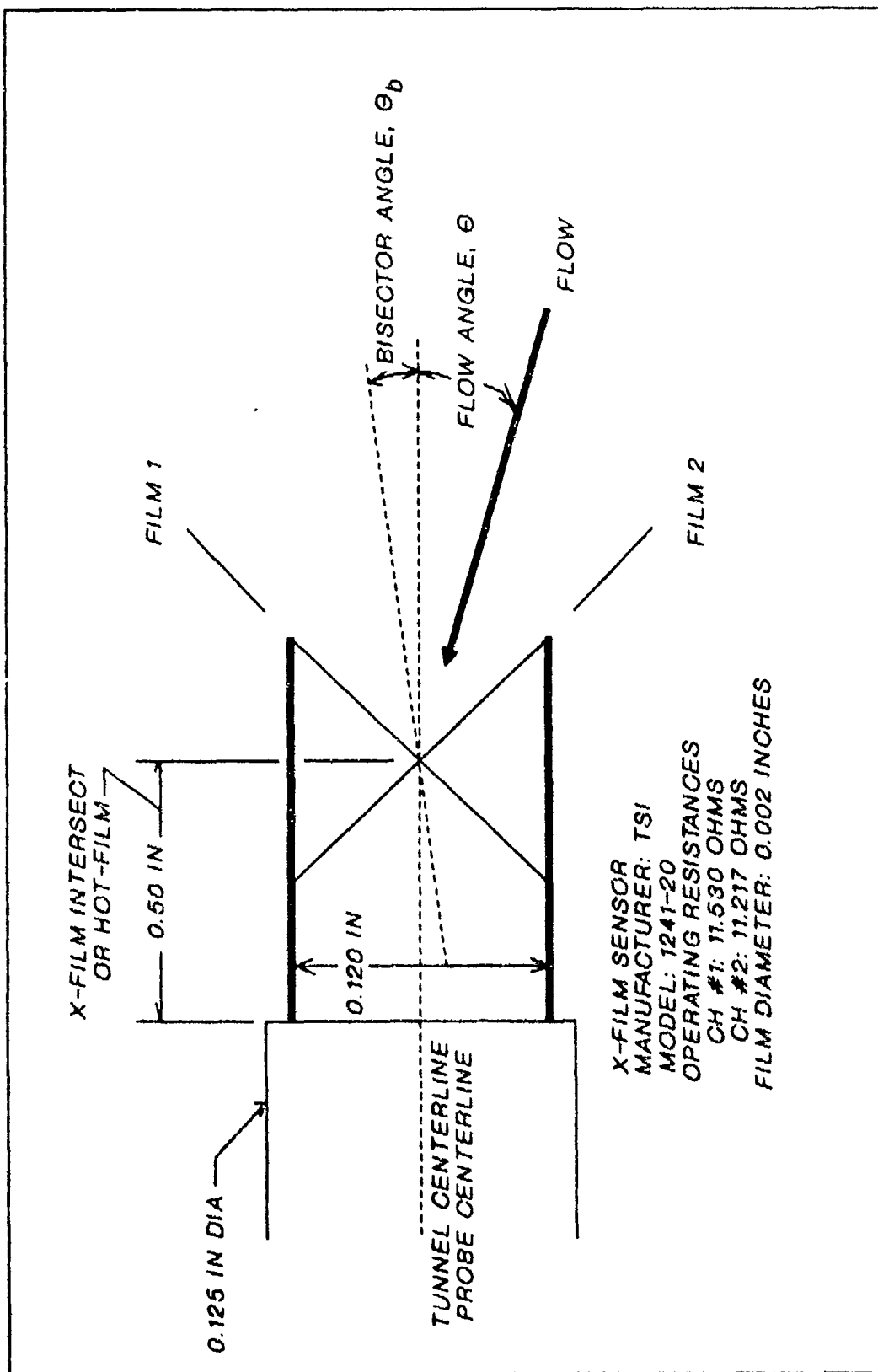


Figure 1. X-Film

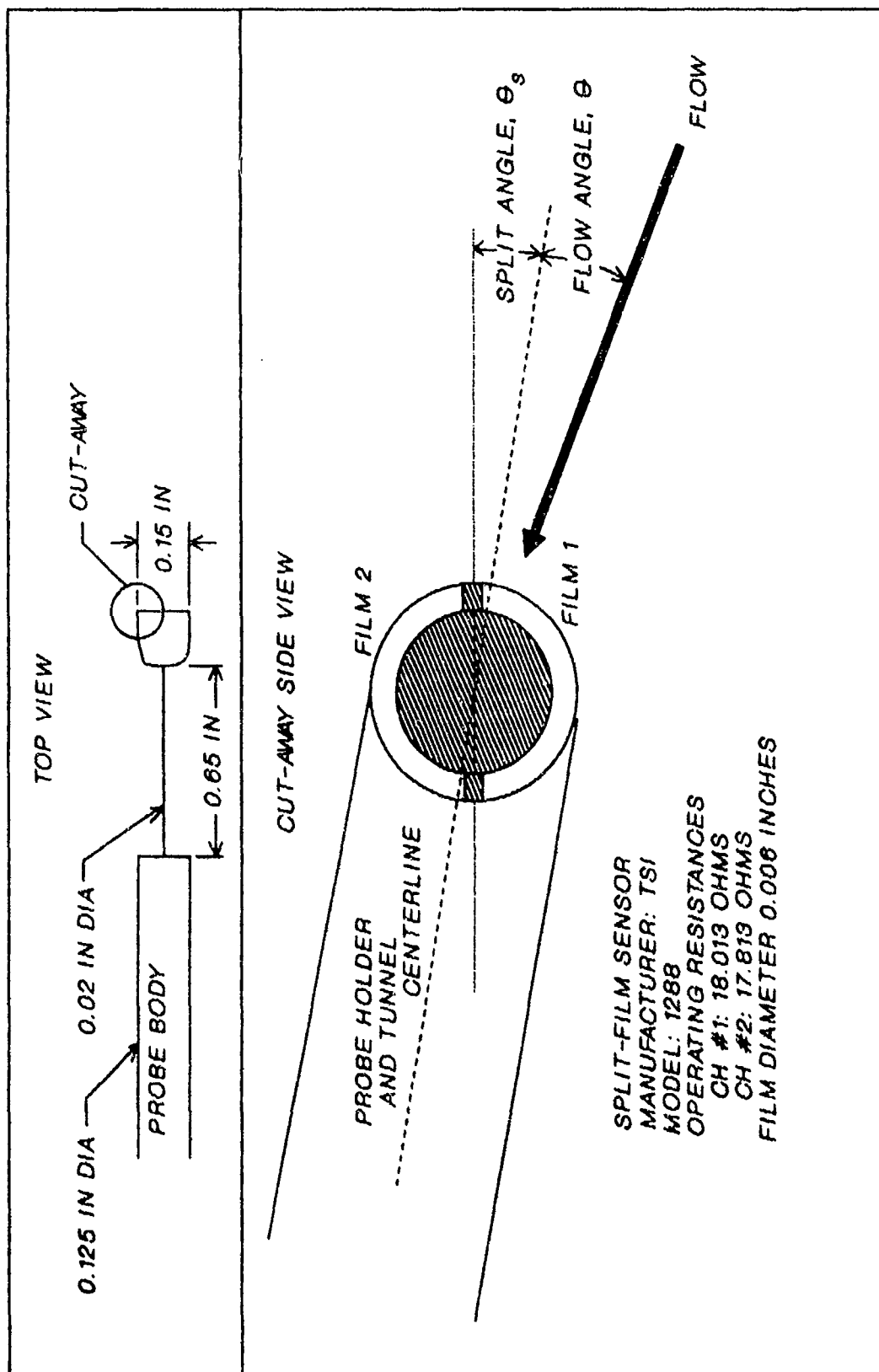


Figure 2. Split-Film

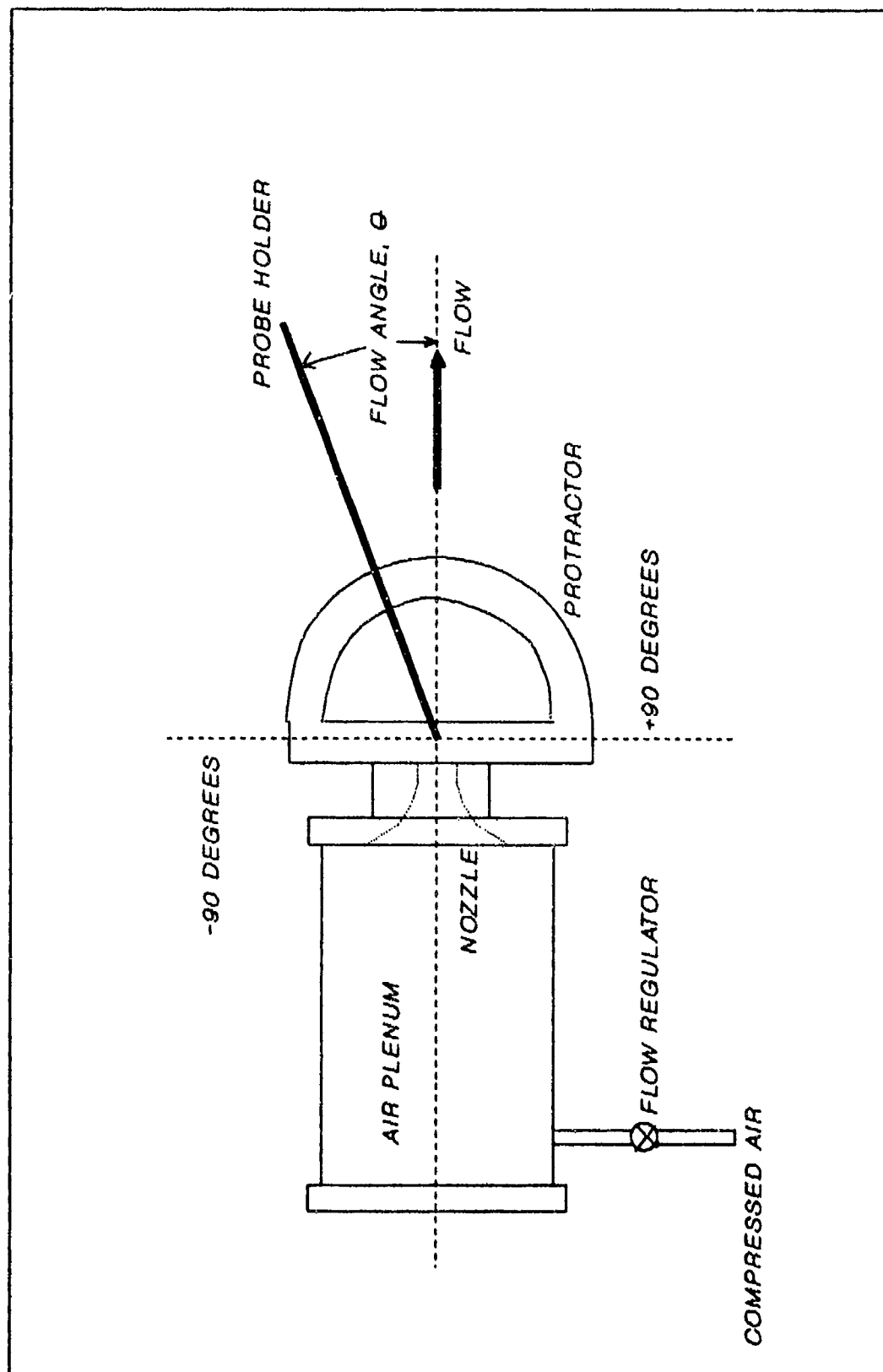
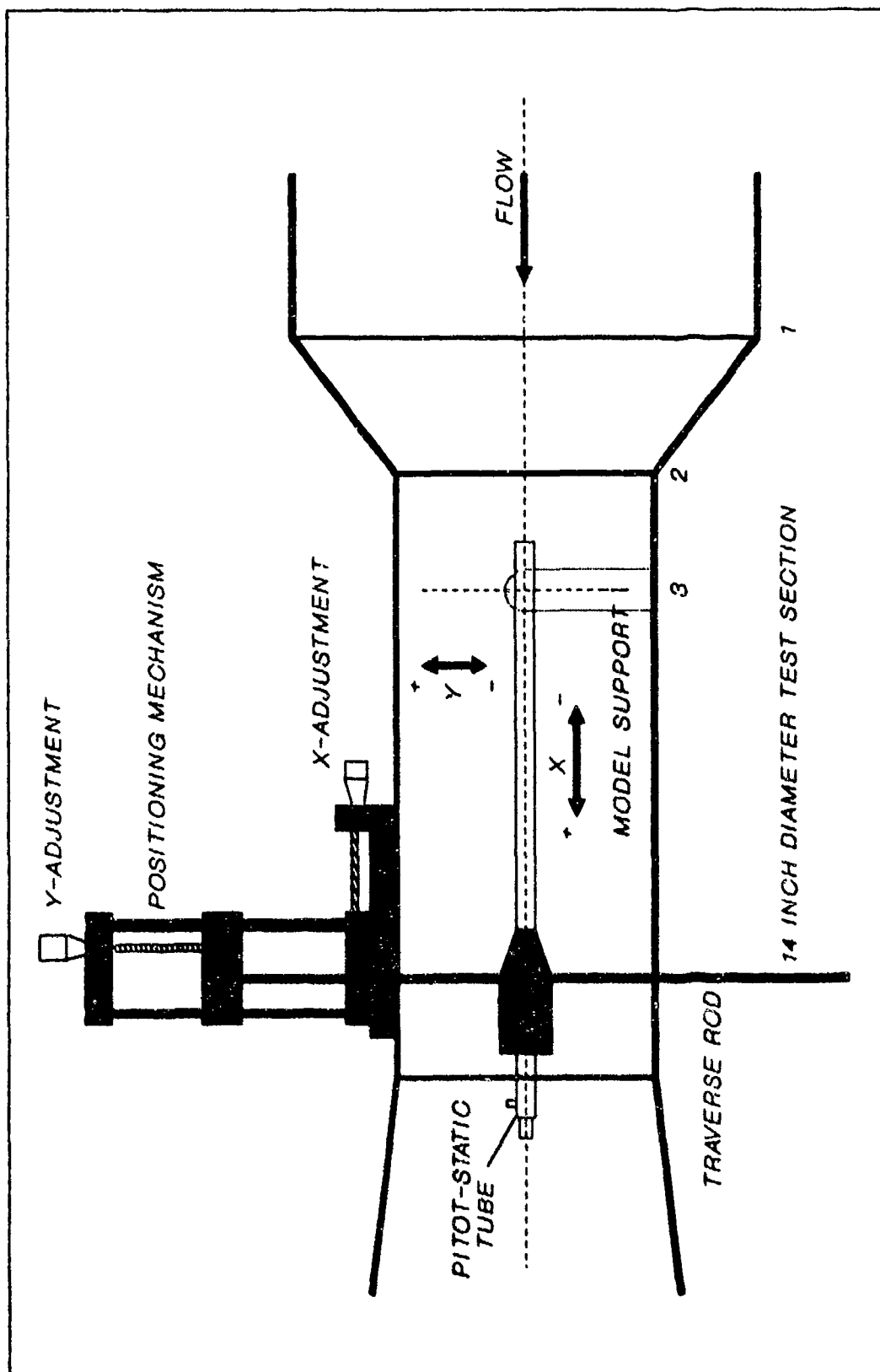


Figure 3. Angle Calibrator



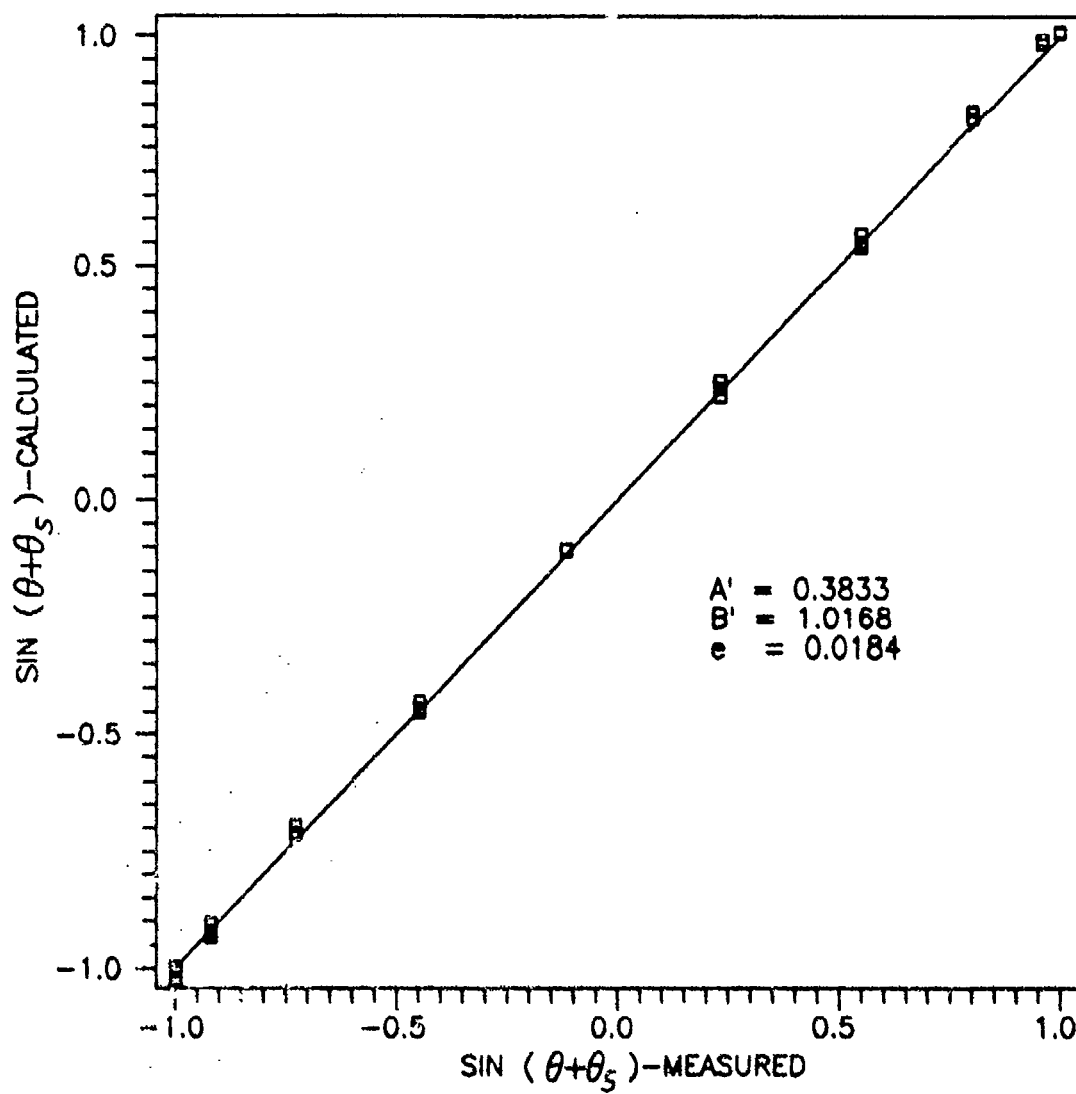


Figure 5. Split-Film Angle Calibration

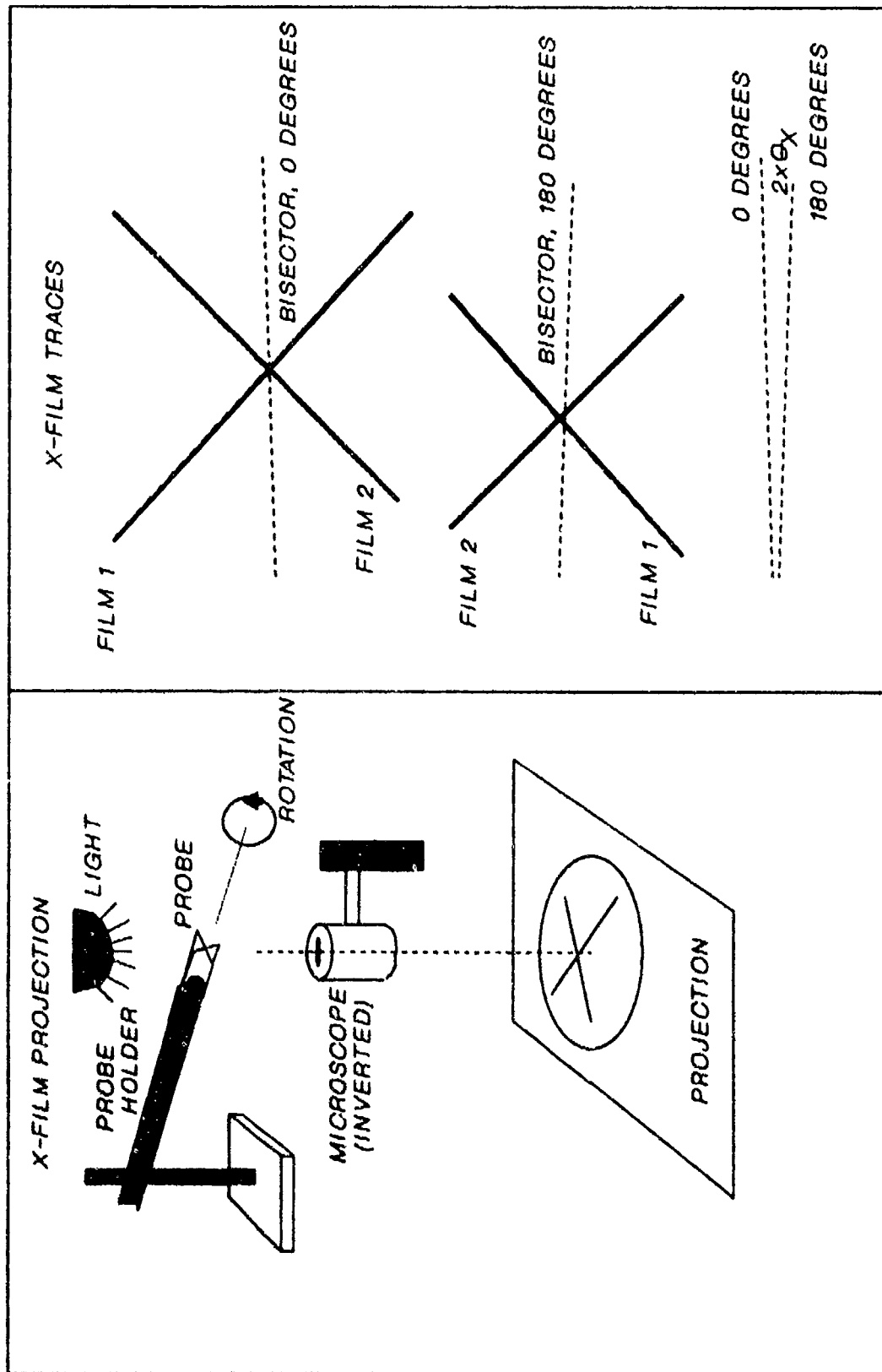


Figure 6. X-Film Bisector Angle



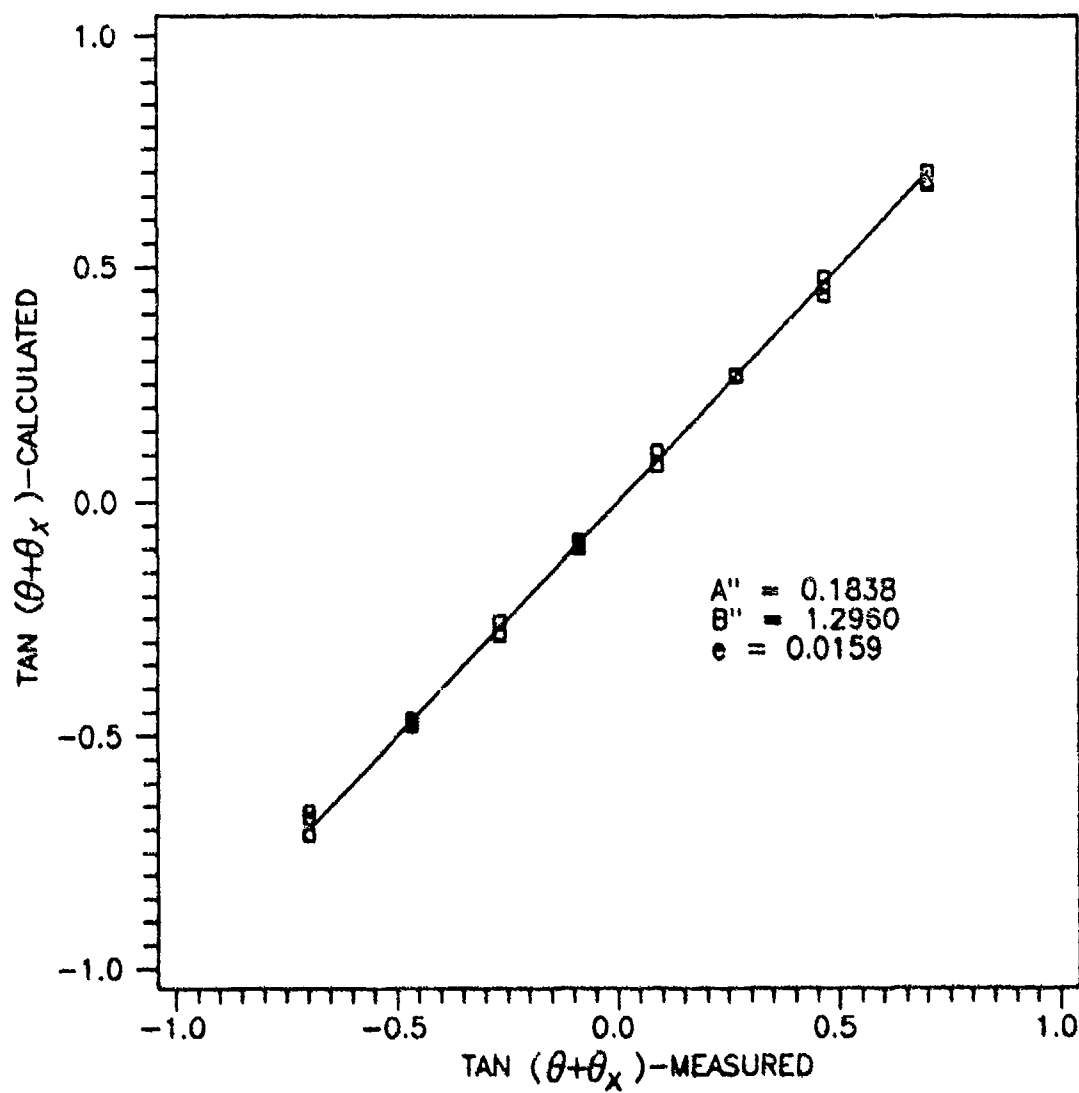


Figure 7. X-Film Angle Calibration

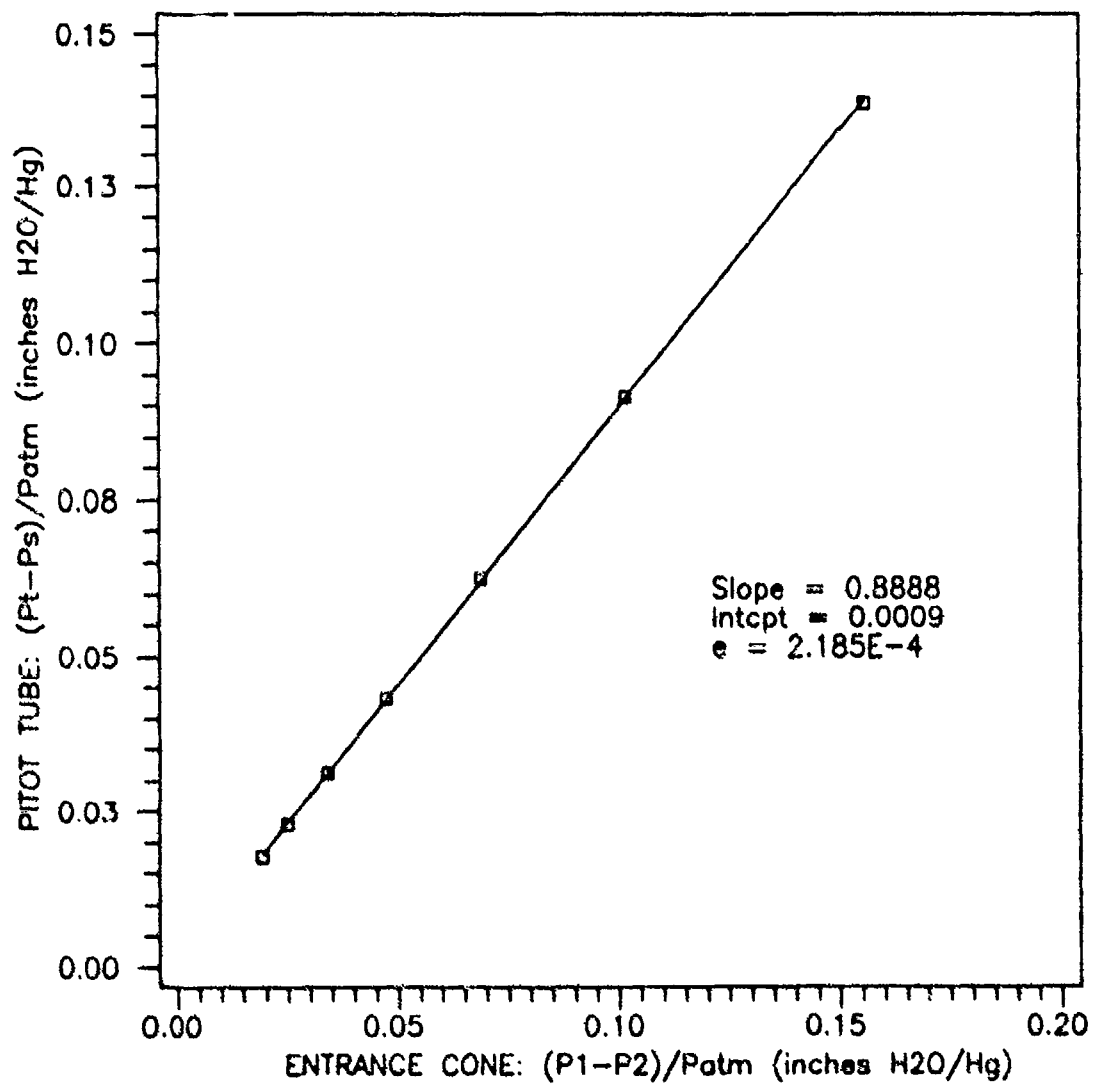


Figure B. Tunnel Velocity Calibration

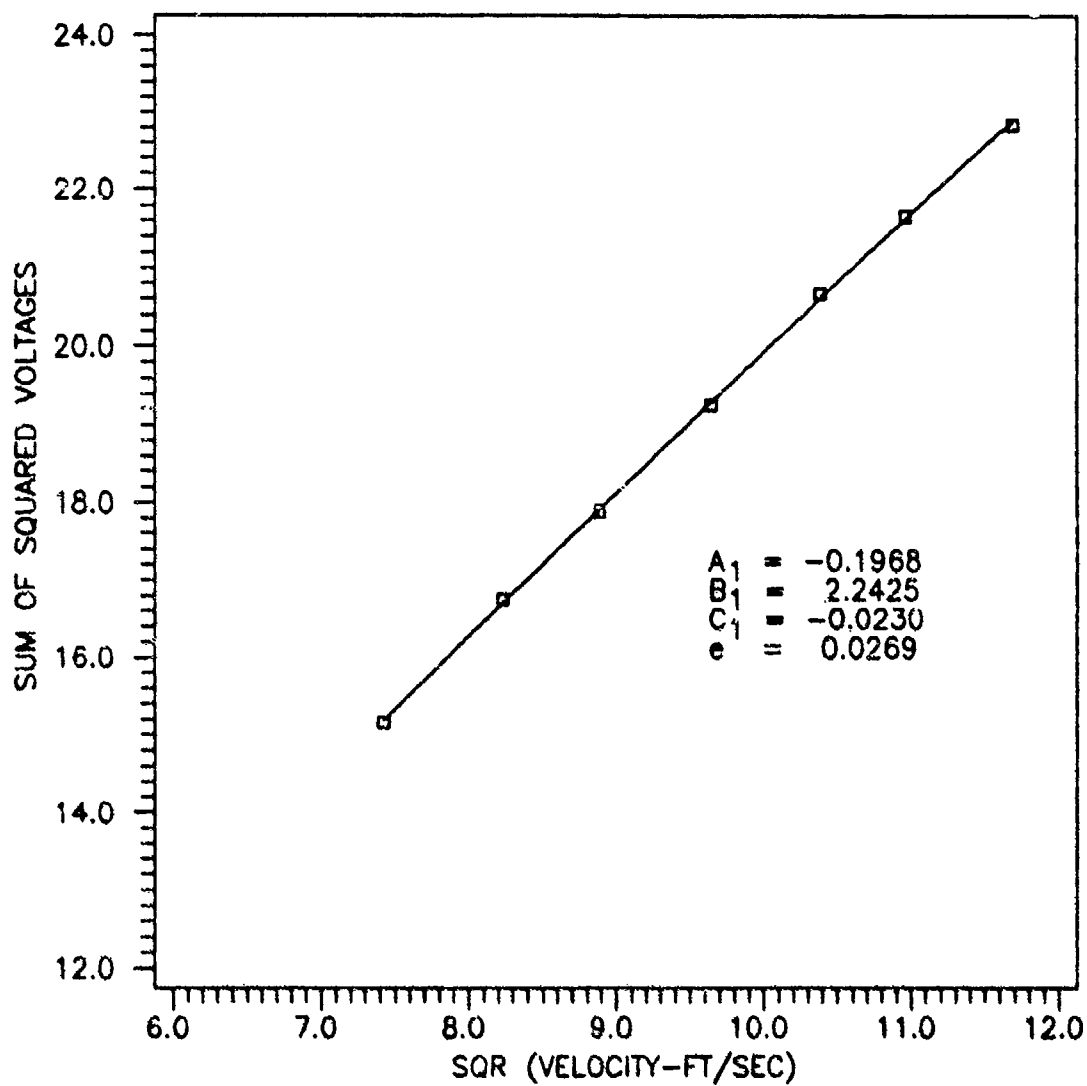


Figure 9. Split-Film Velocity Calibration

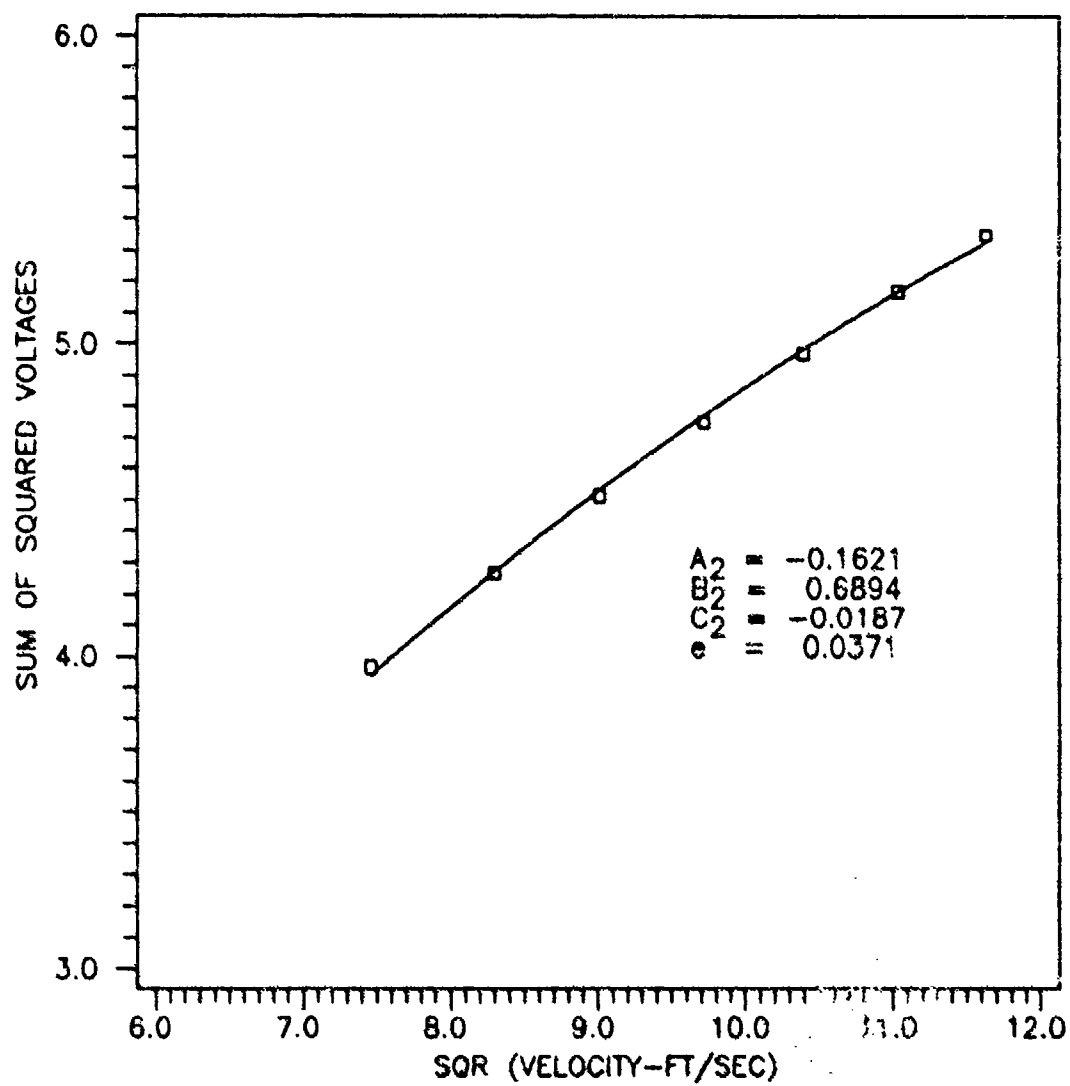


Figure 10. X-Film Velocity Calibration

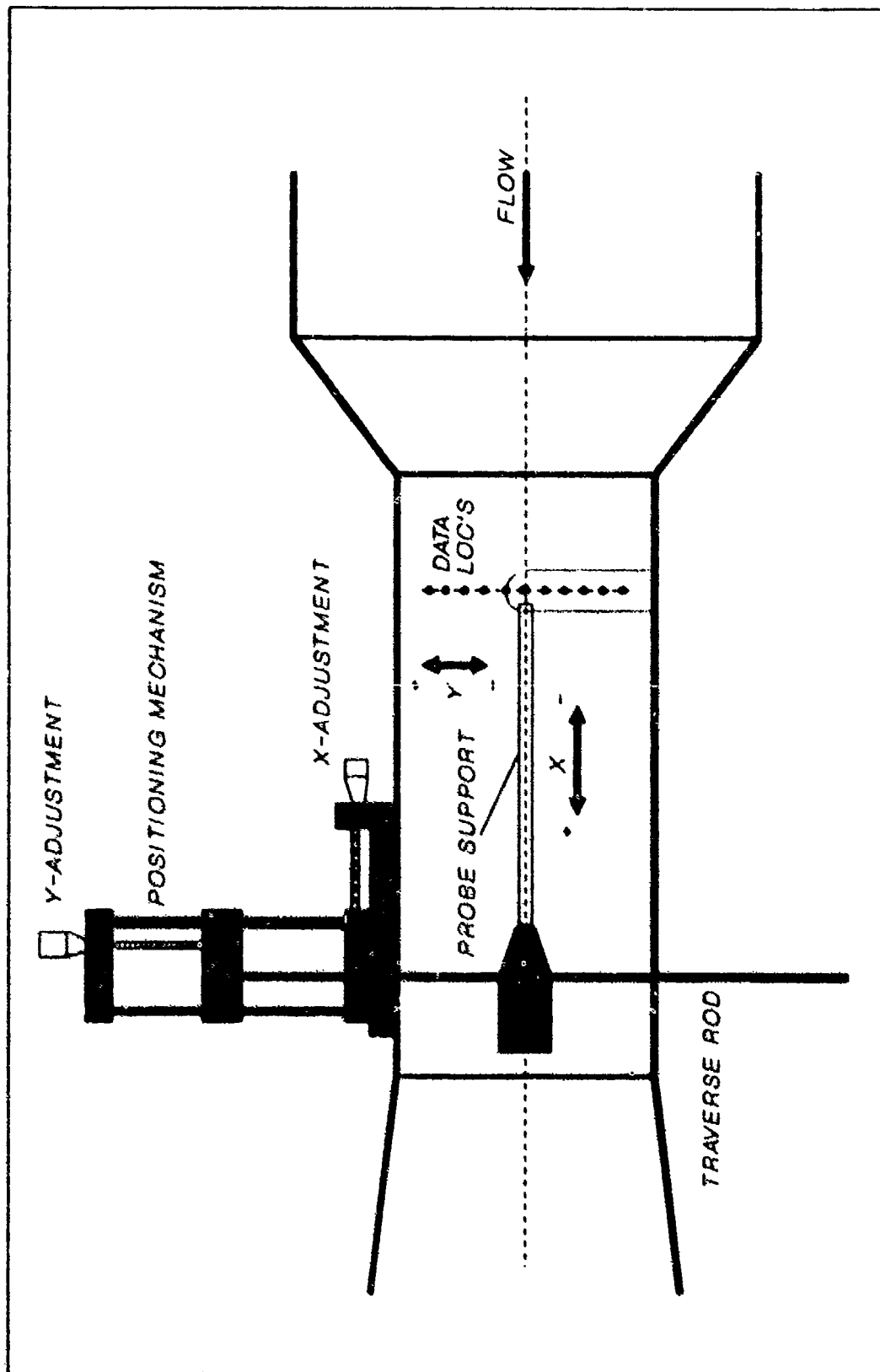


Figure 11. Open Tunnel Data Retrieval

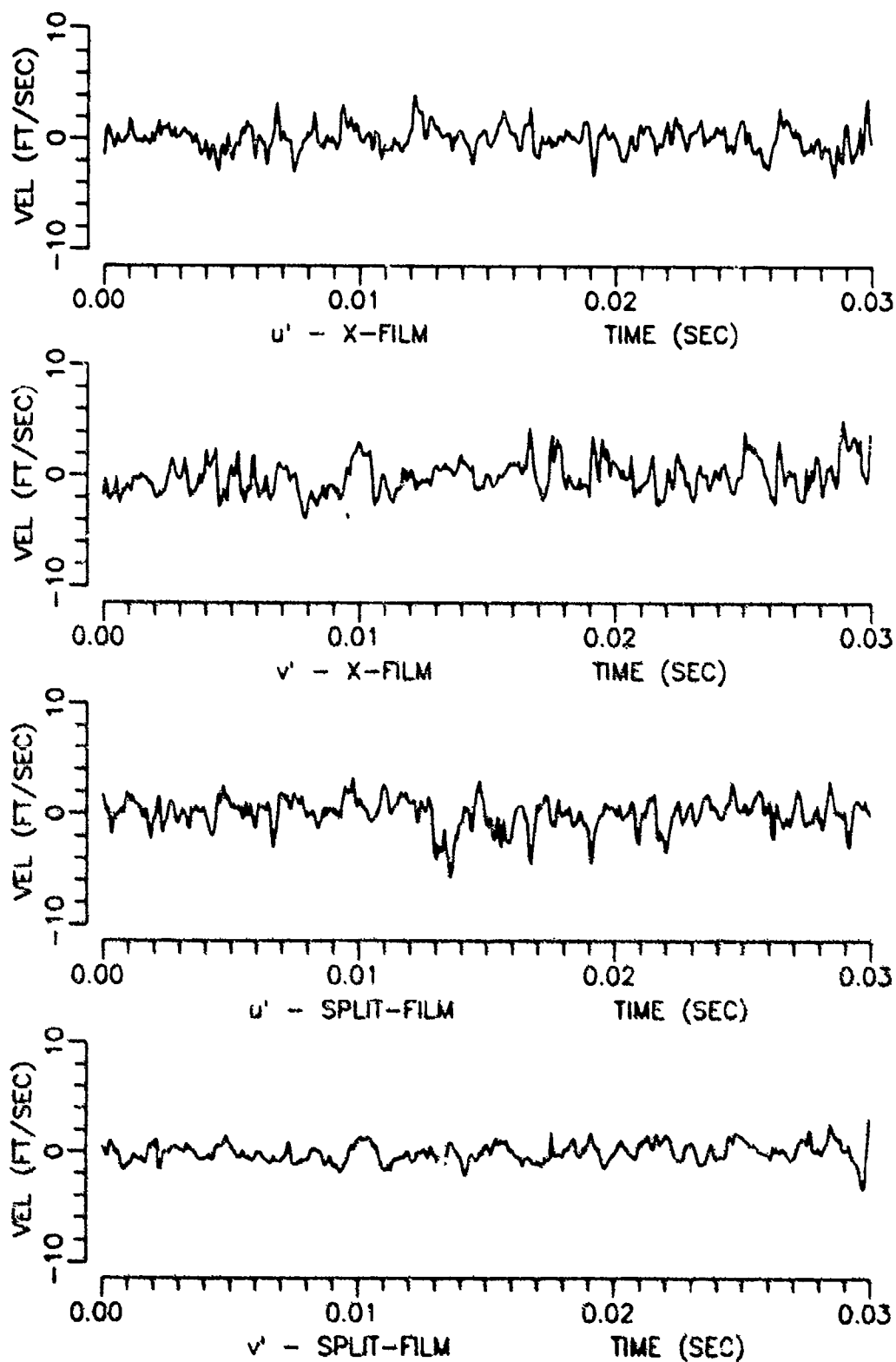


Figure 12. Split-Film and X-Film  $u'$  and  $v'$ , open Tunnel Centerline (Vel=122 Ft/sec)

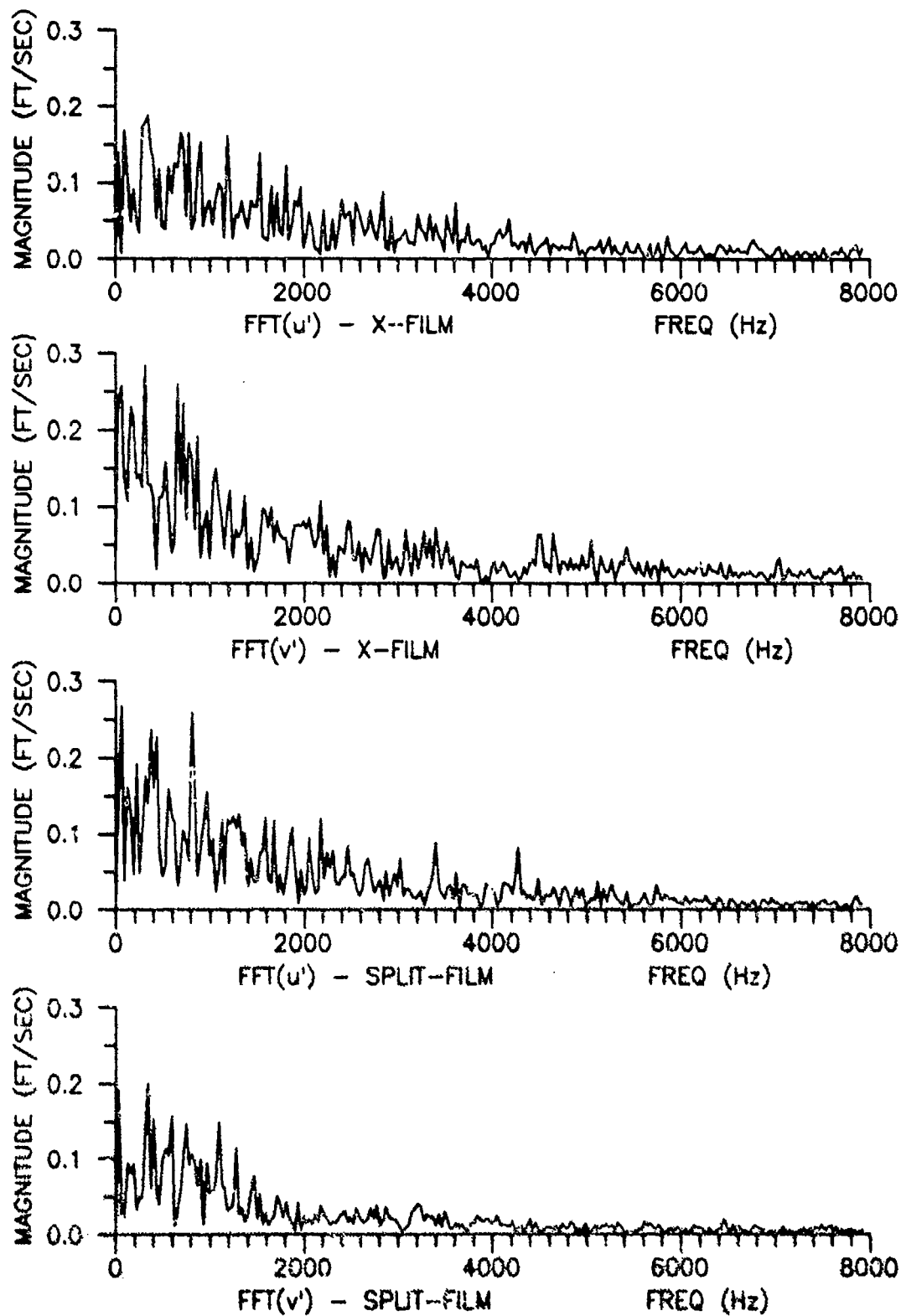


Figure 13. Split-Film and X-Film FFT(u') and FFT (v').  
Open Tunnel Centerline (Vel=122 Ft/sec)

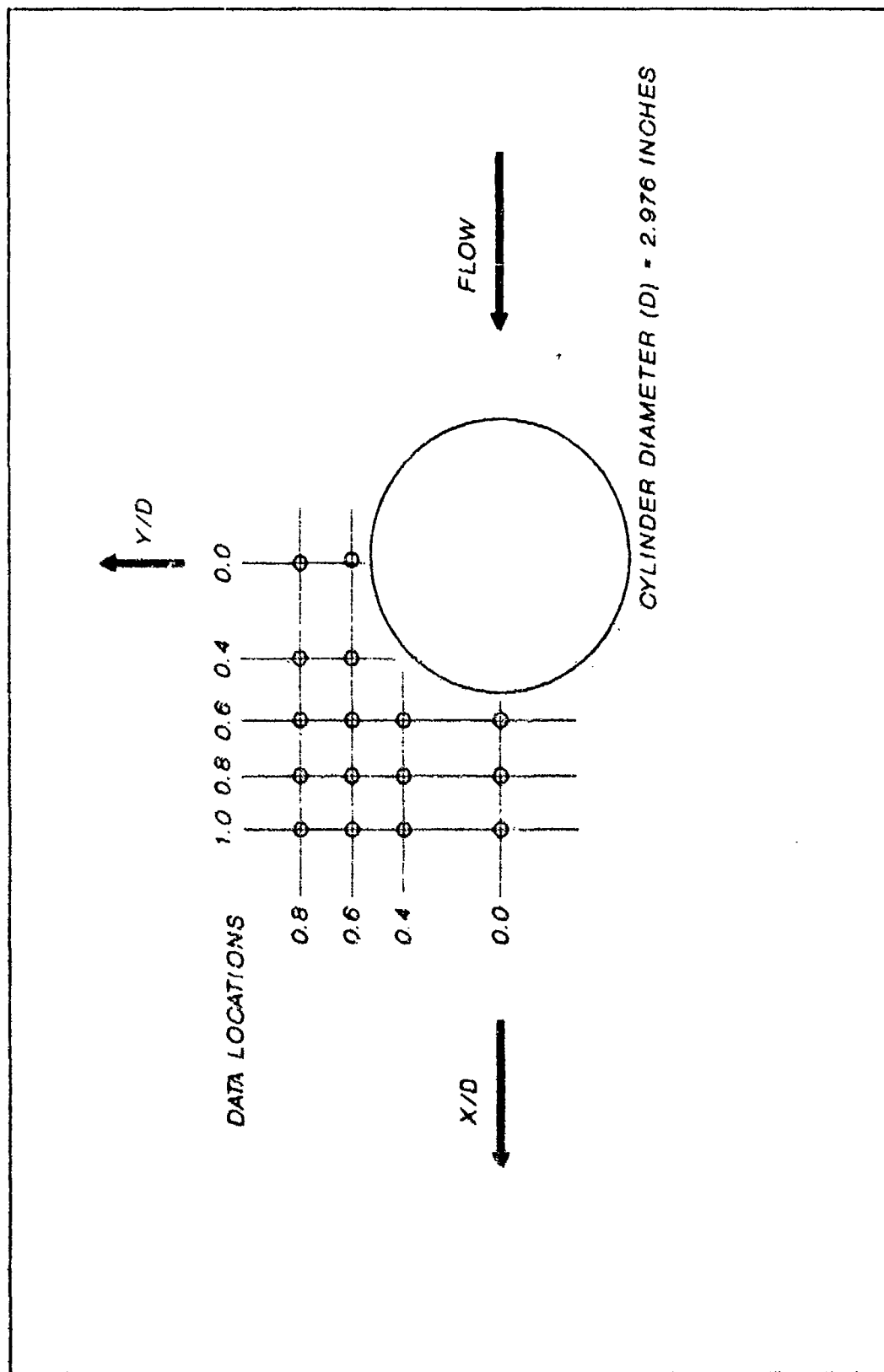


Figure 14. Cylinder Data Retrieval



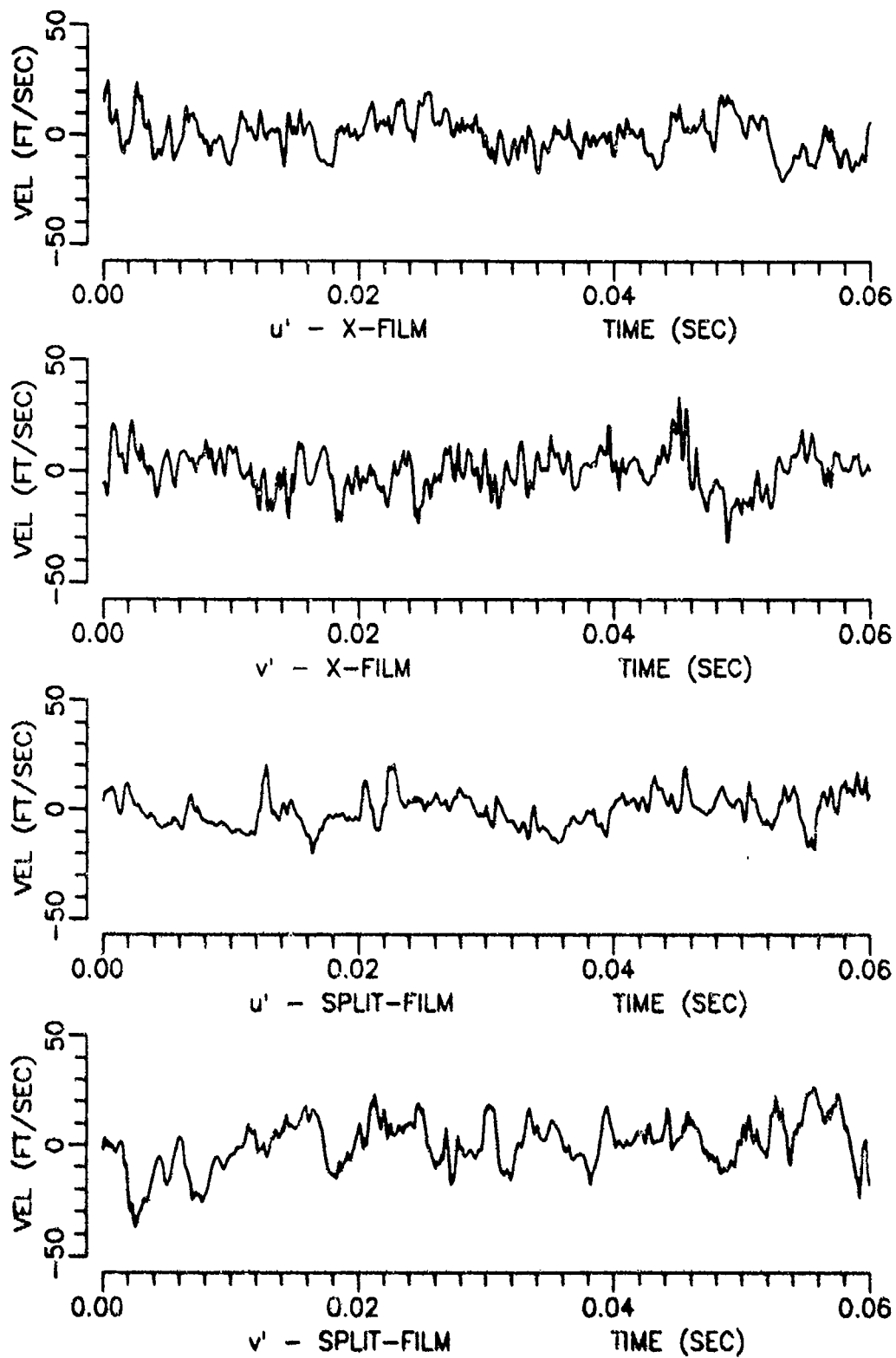


Figure 15. Split-Film and X-Film  $u'$  and  $v'$ , Behind Cylinder  
 $X/D=0.6$ ,  $Y/D=0.0$  ( $Re = 144,000$ )

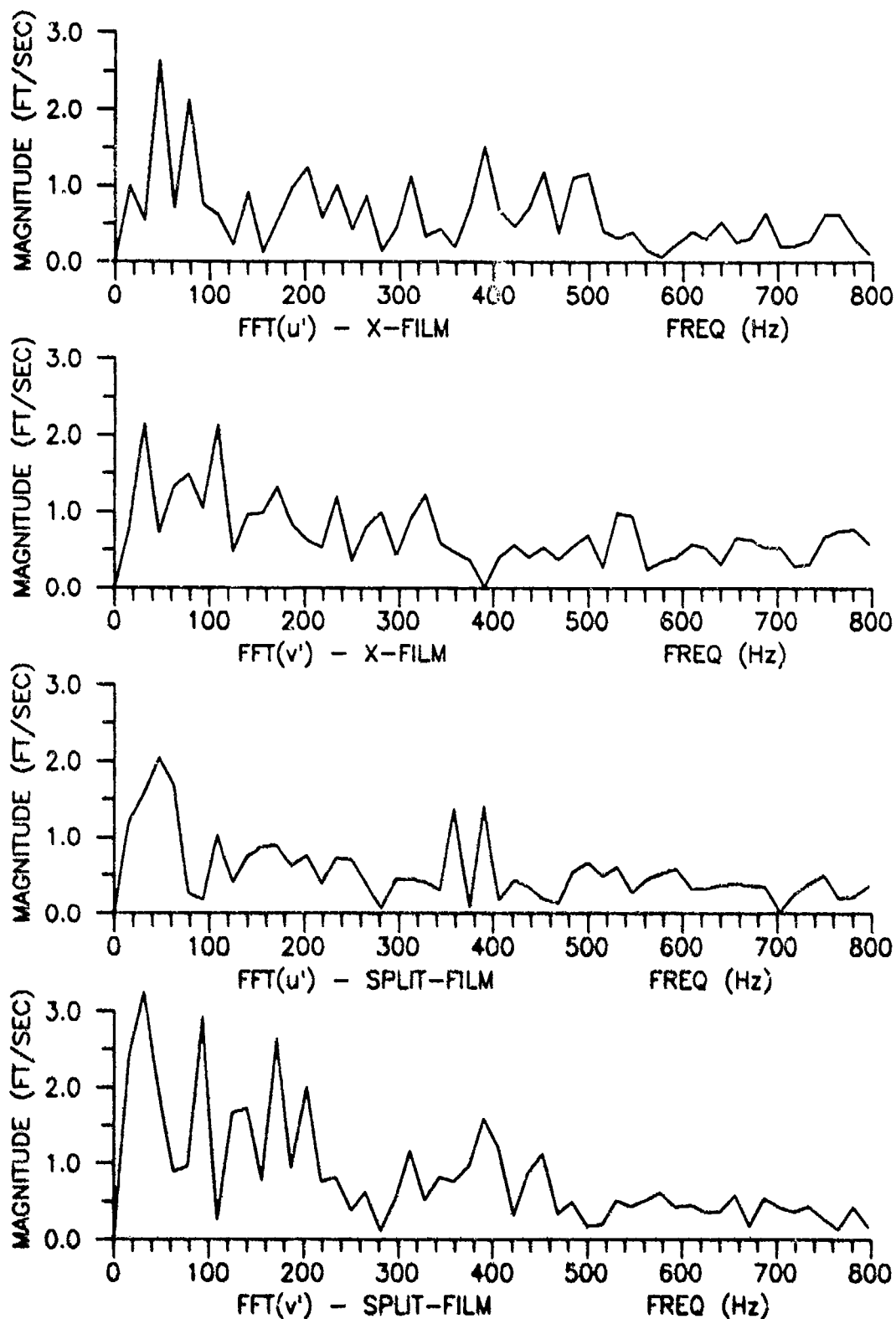


Figure 16. Split-Film and X-Film  $FFT(u')$  and  $FFT(v')$ ,  
Behind Cylinder,  $X/D=0.6$ ,  $Y/D=0.0$  ( $Re = 144,000$ )

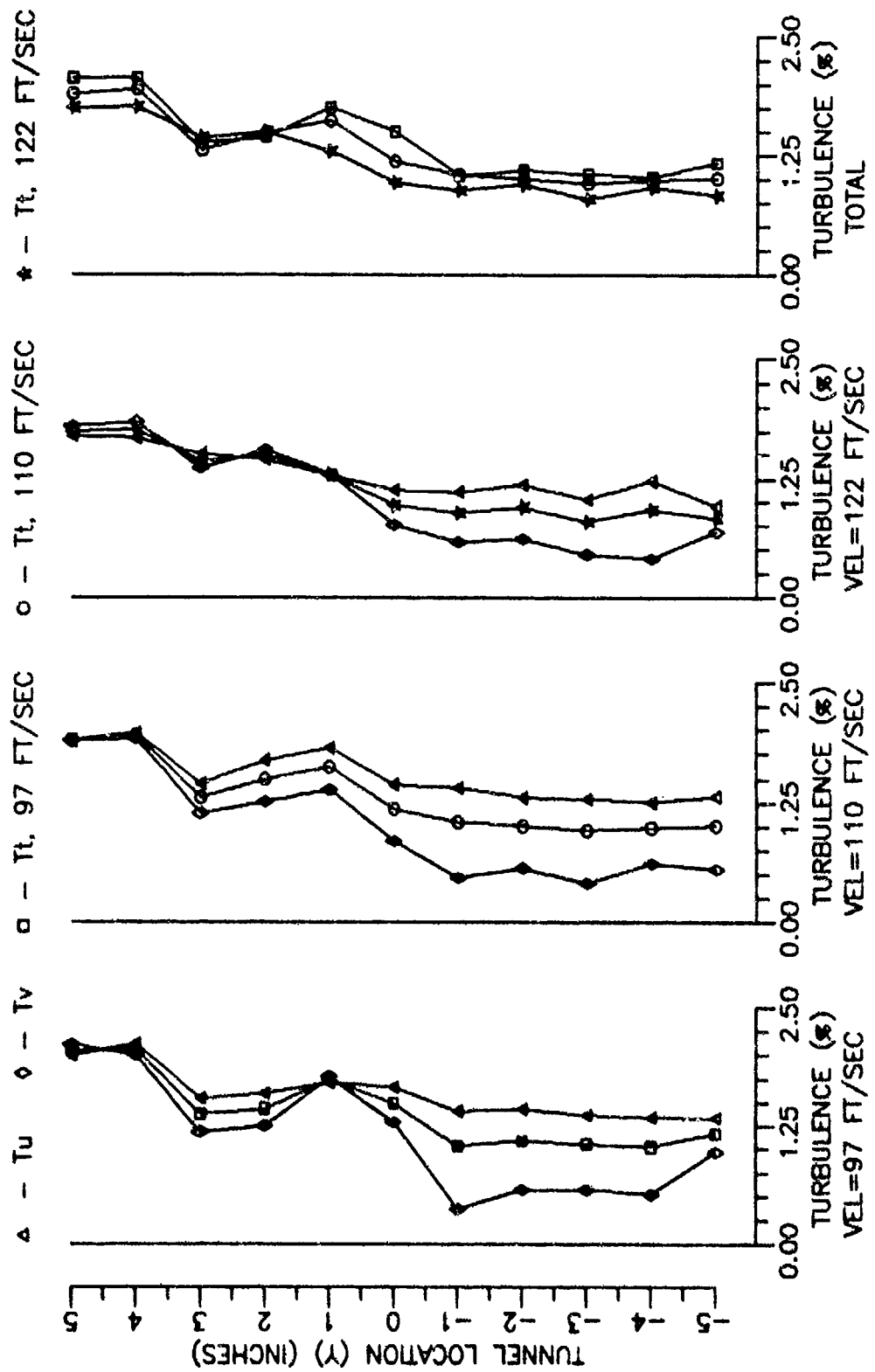


Figure 17. Split-Film Turbulence, Open Tunnel

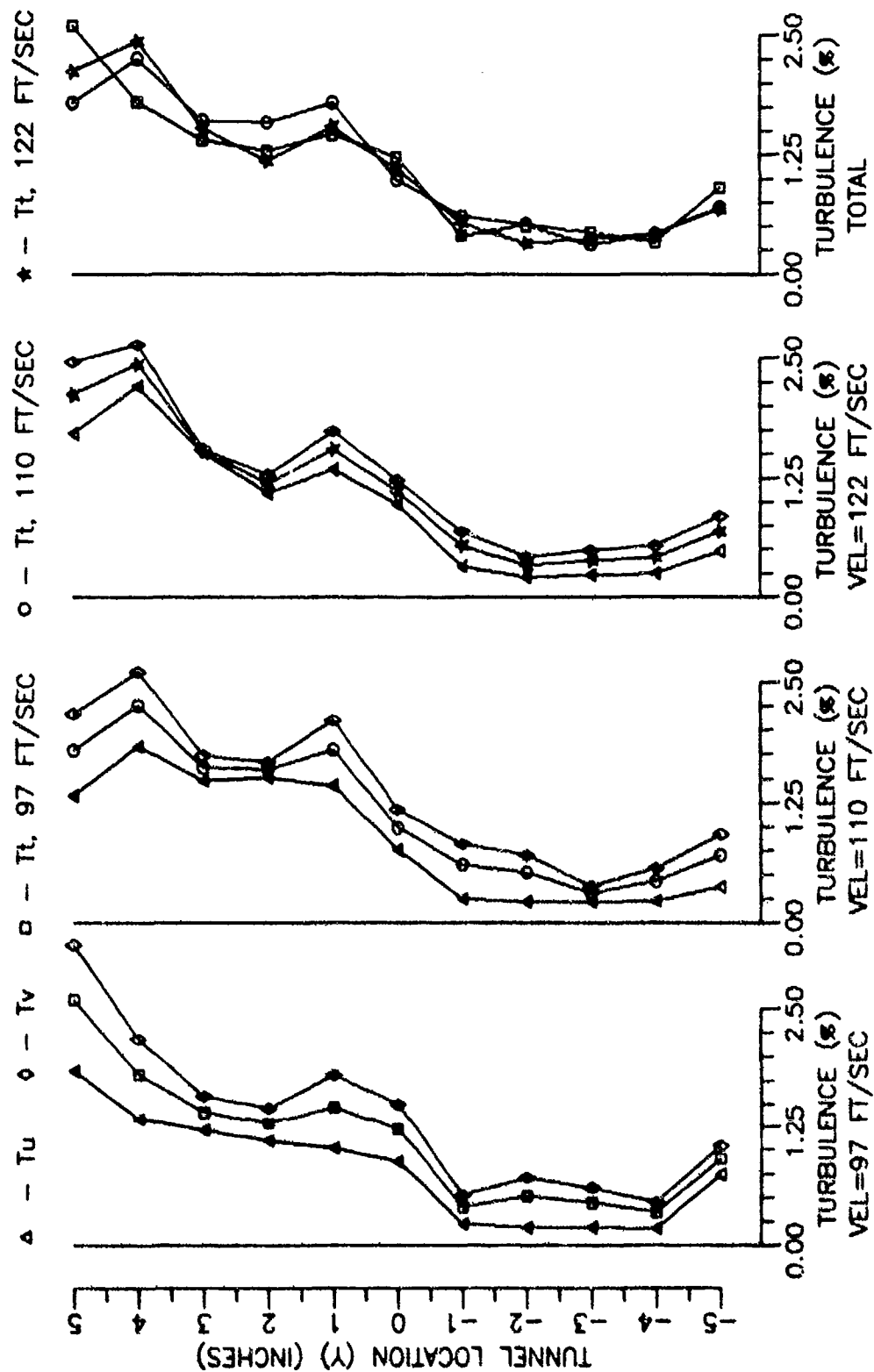


Figure 18. X-Film Turbulence, Open Tunnel

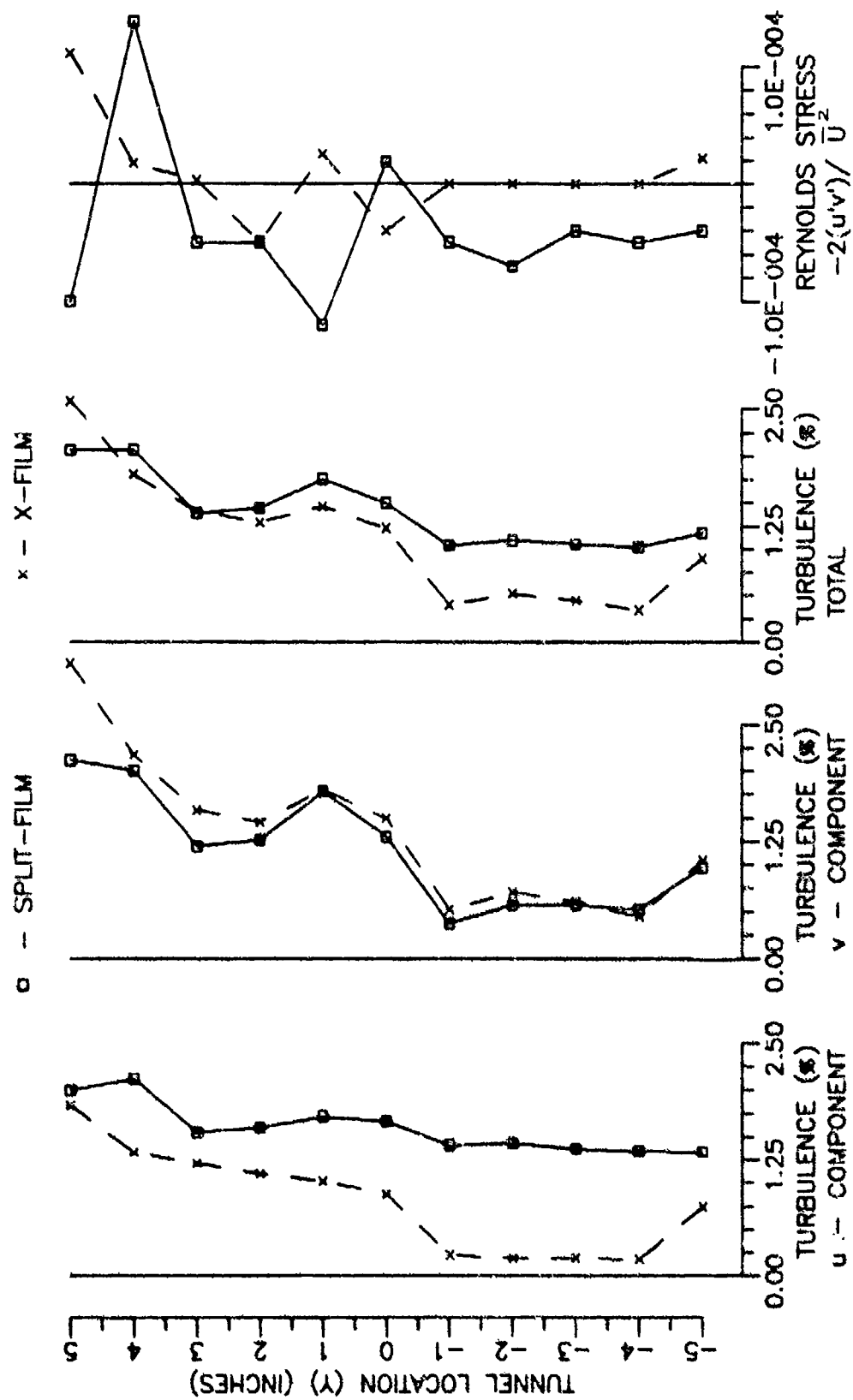


Figure 19. Split-Film vs X-Film Turbulence, Open Tunnel (VEL=97 FT/SEC)

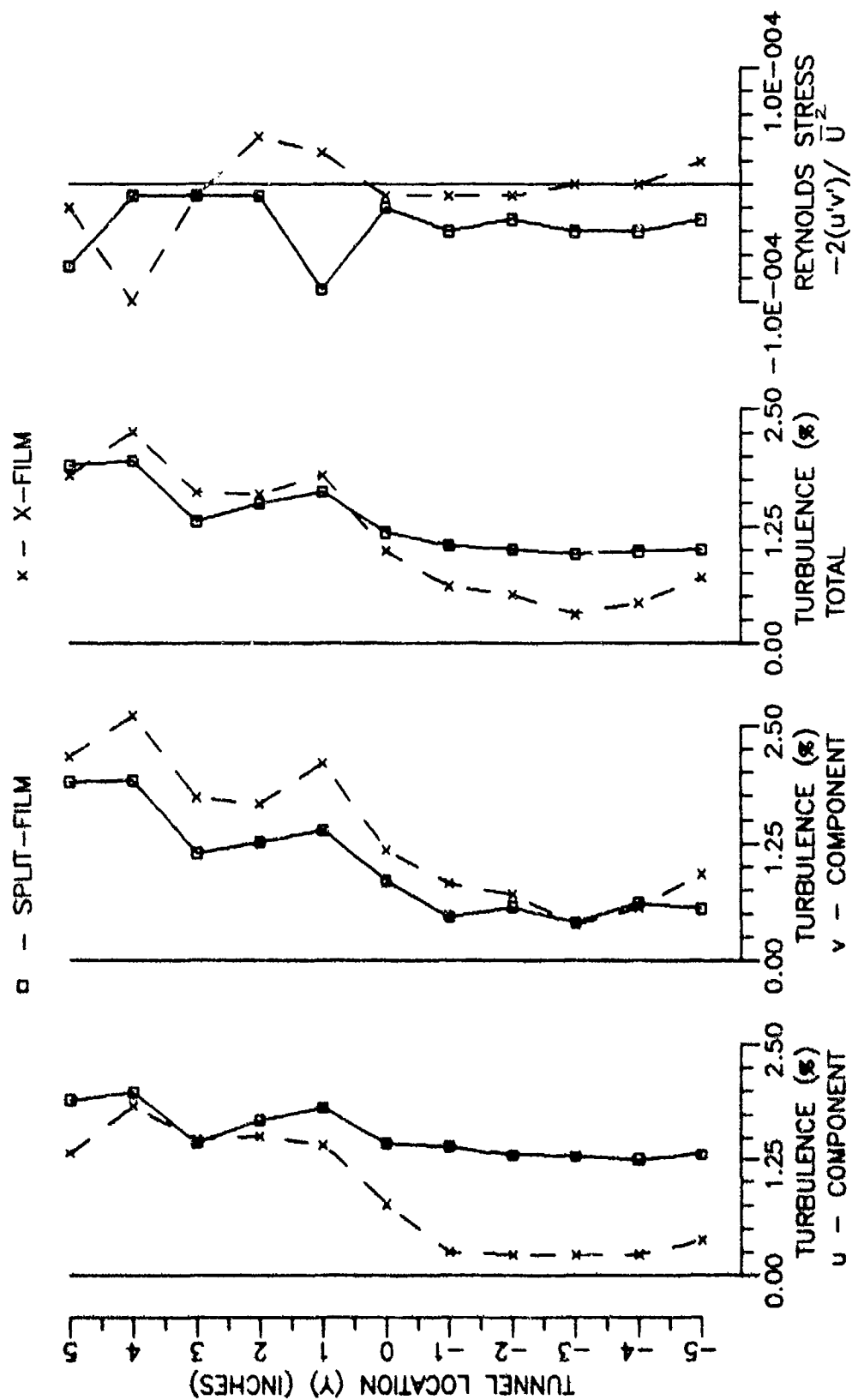


Figure 20. Split-Film vs X-Film Turbulence, Open Tunnel (VEL=110 FT/SEC)

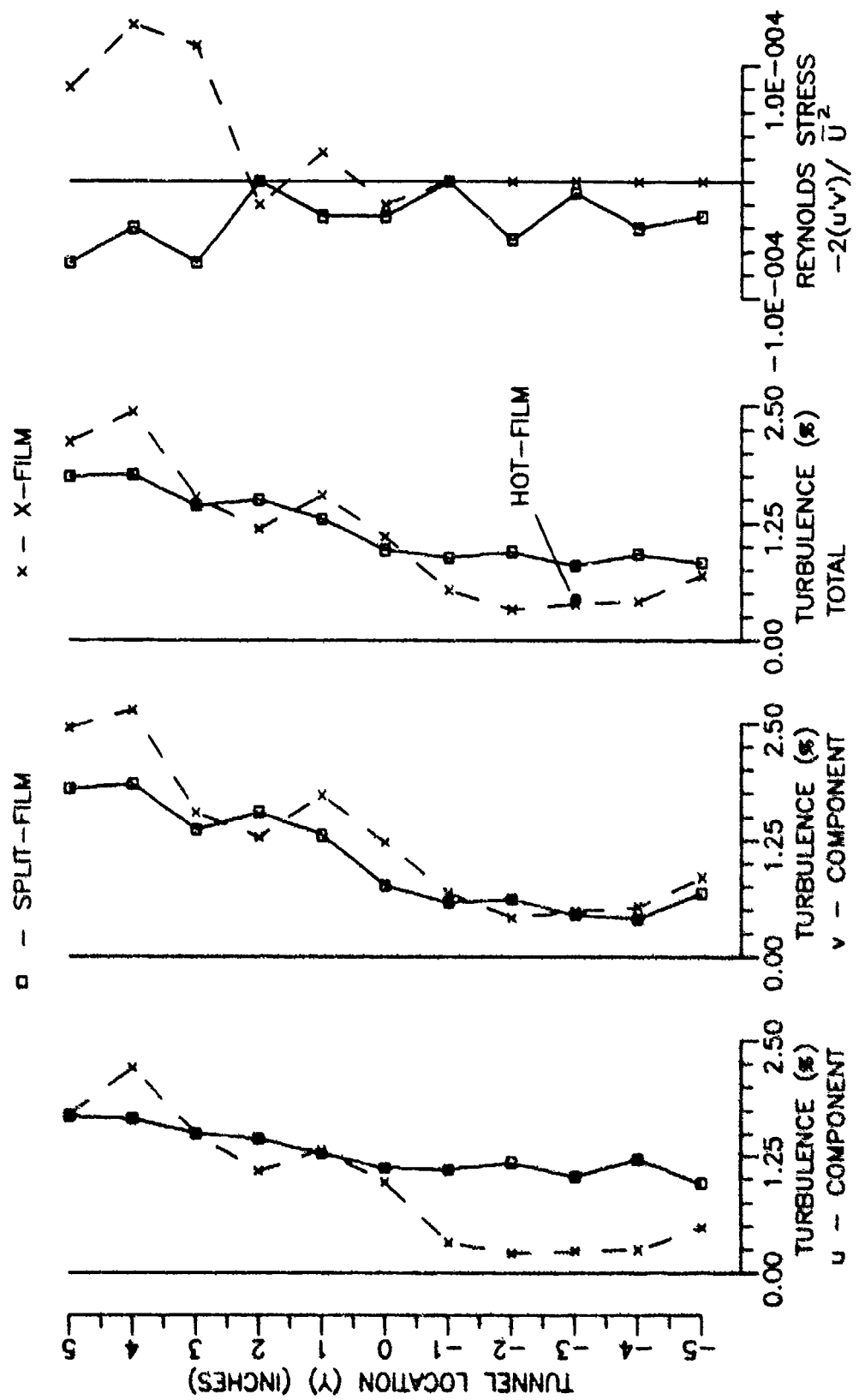


Figure 21. Split-Film vs X-Film Turbulence, Open Tunnel (VEL=122 FT/SEC)

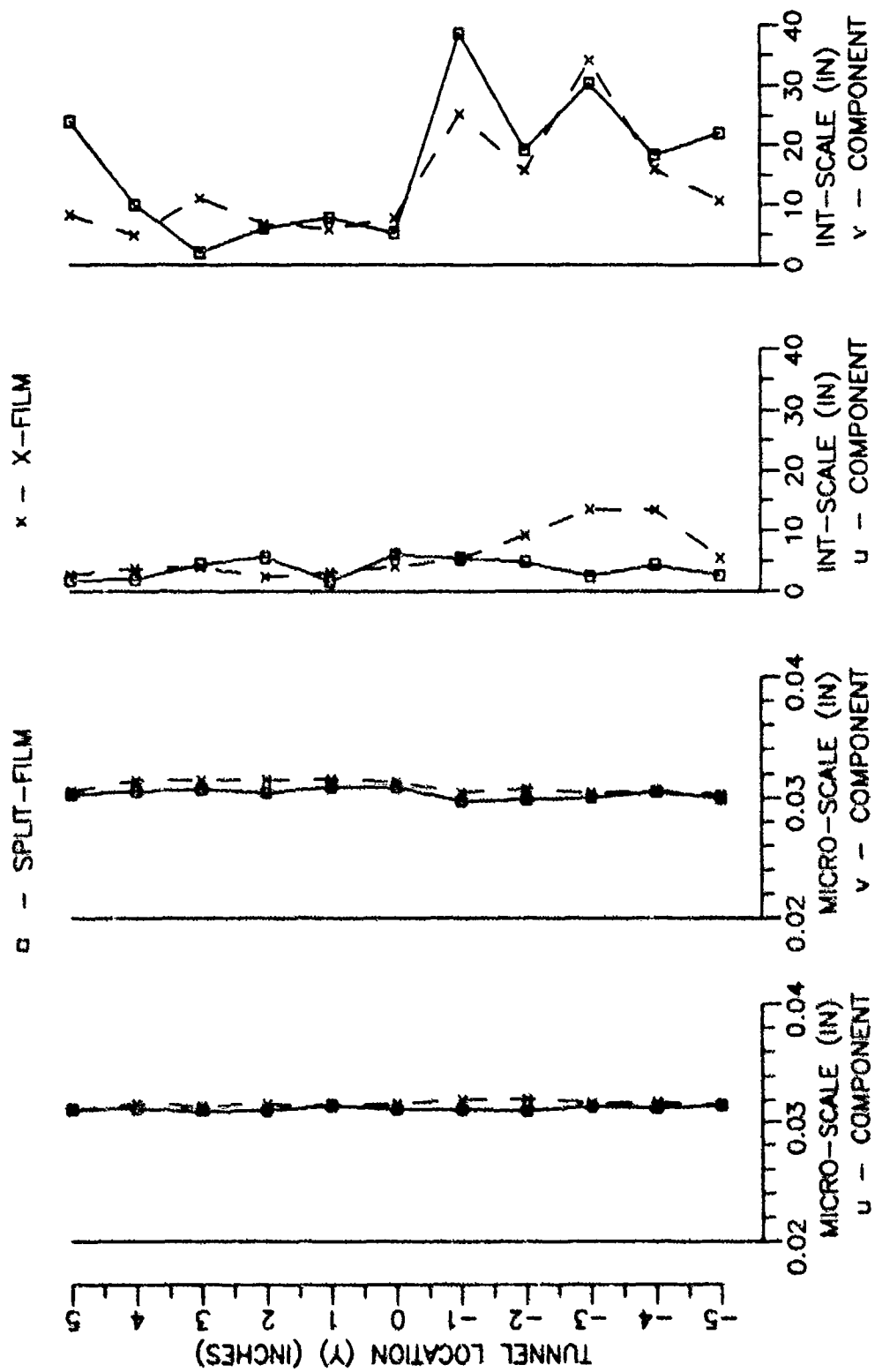


Figure 22. Turbulence Scales, Open Tunnel (VEL=122 FT/SEC)



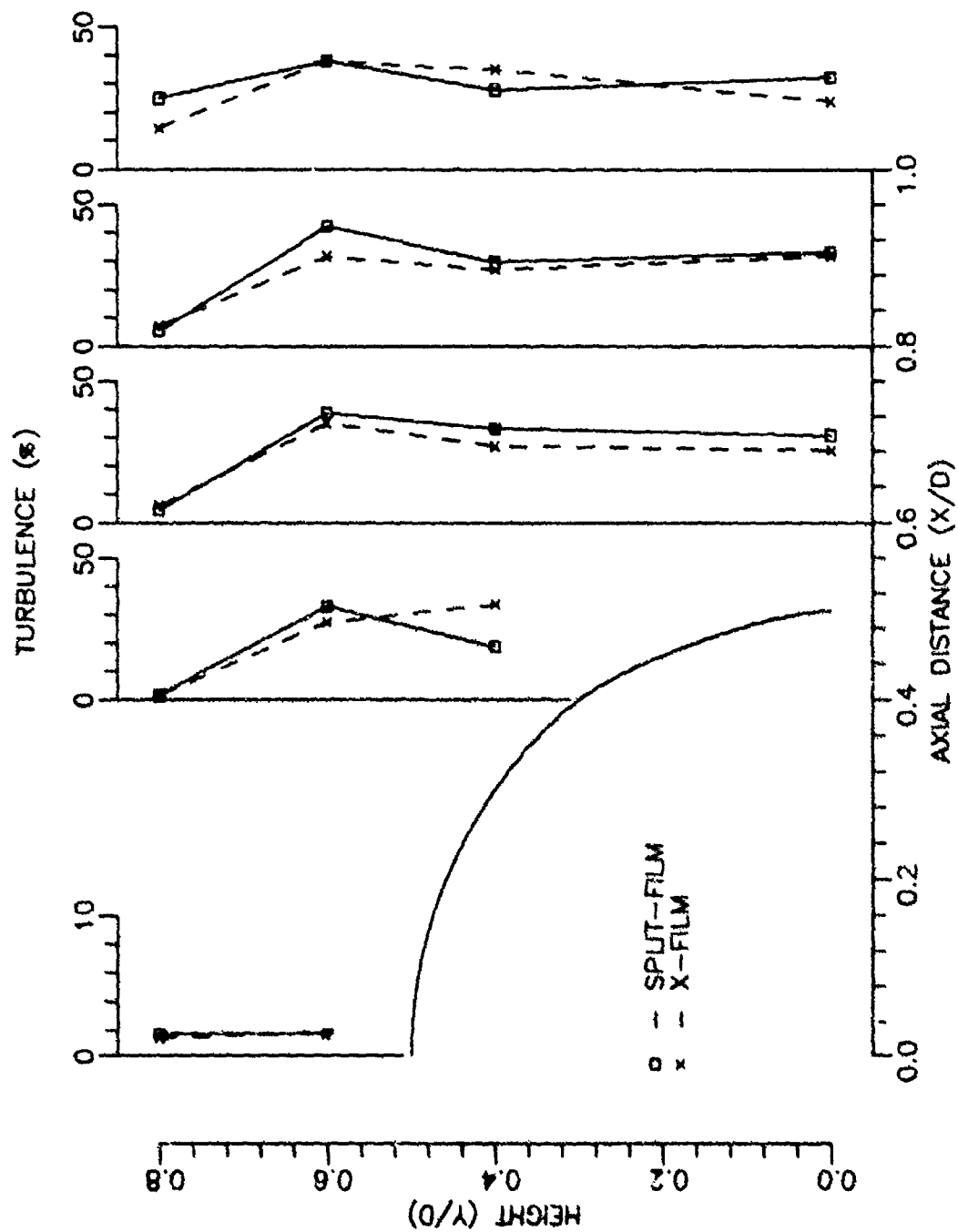


Figure 23. Turbulence Intensity Behind Cylinder, u-Component ( $Re = 144,000$ )

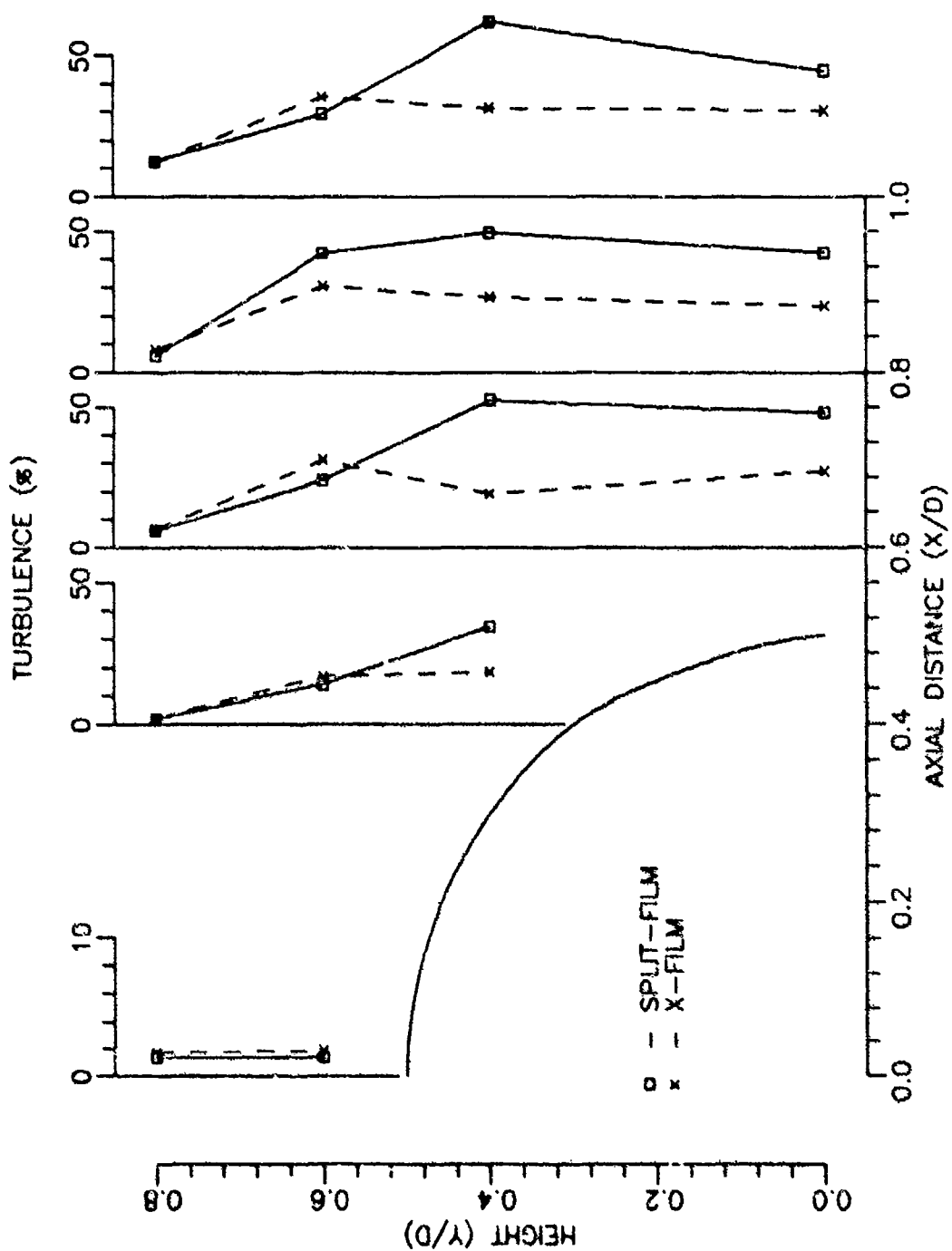


Figure 24. Turbulence Intensity Behind Cylinder, v-Component ( $Re = 144,000$ )

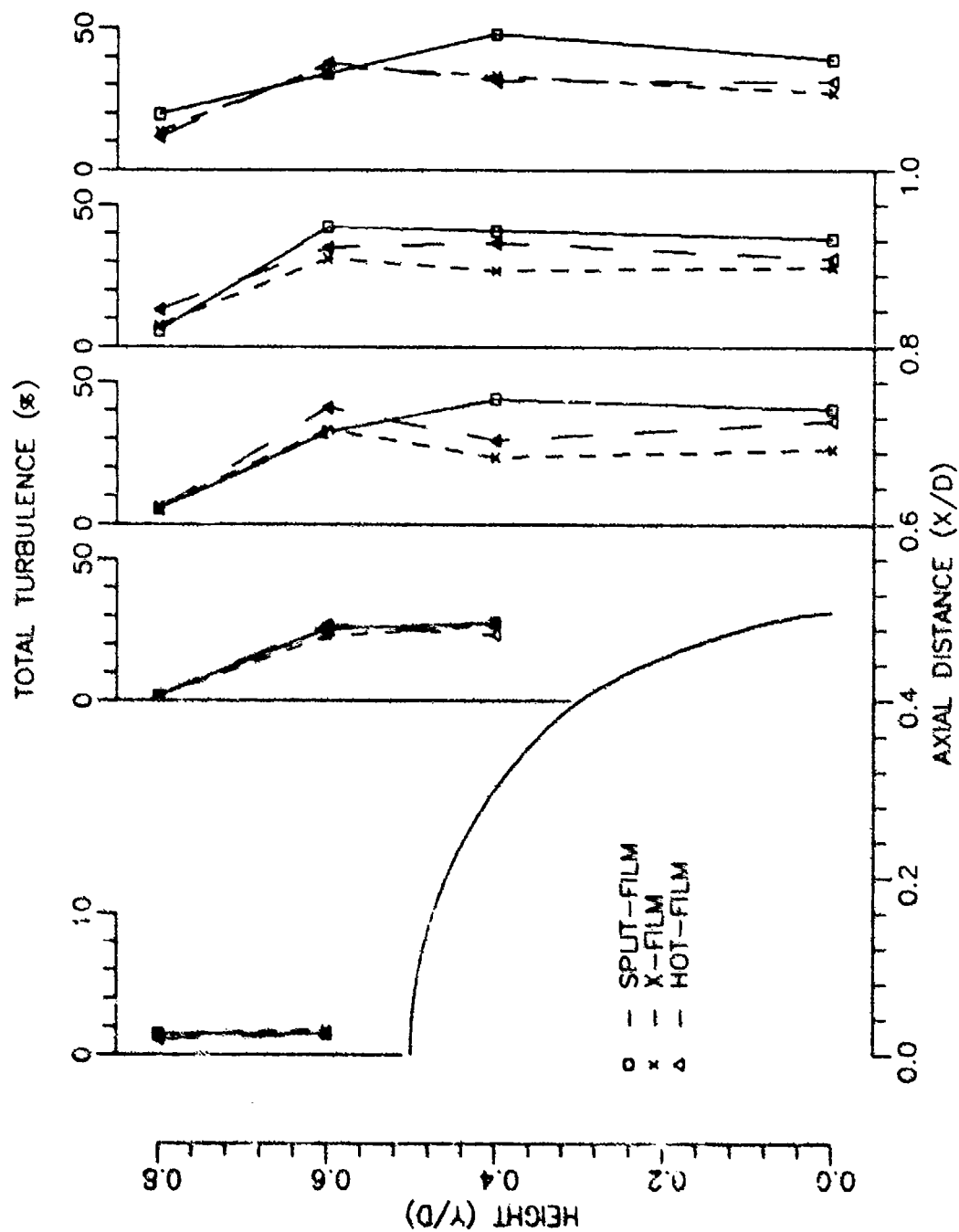


Figure 25. Total Turbulence Intensity Behind Cylinder ( $Re = 144,000$ )

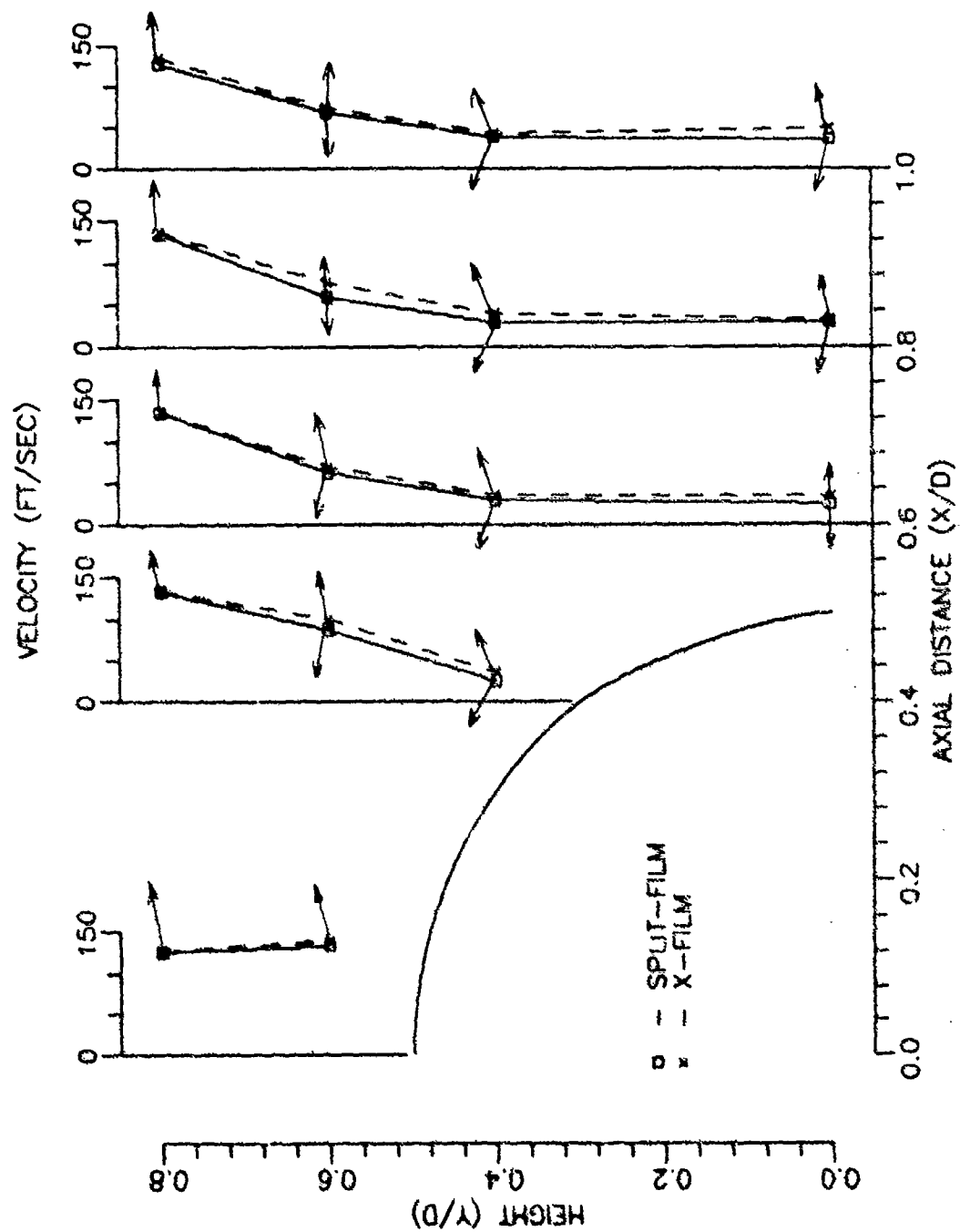


Figure 26. Velocity Behind Cylinder ( $Re = 144,000$ )

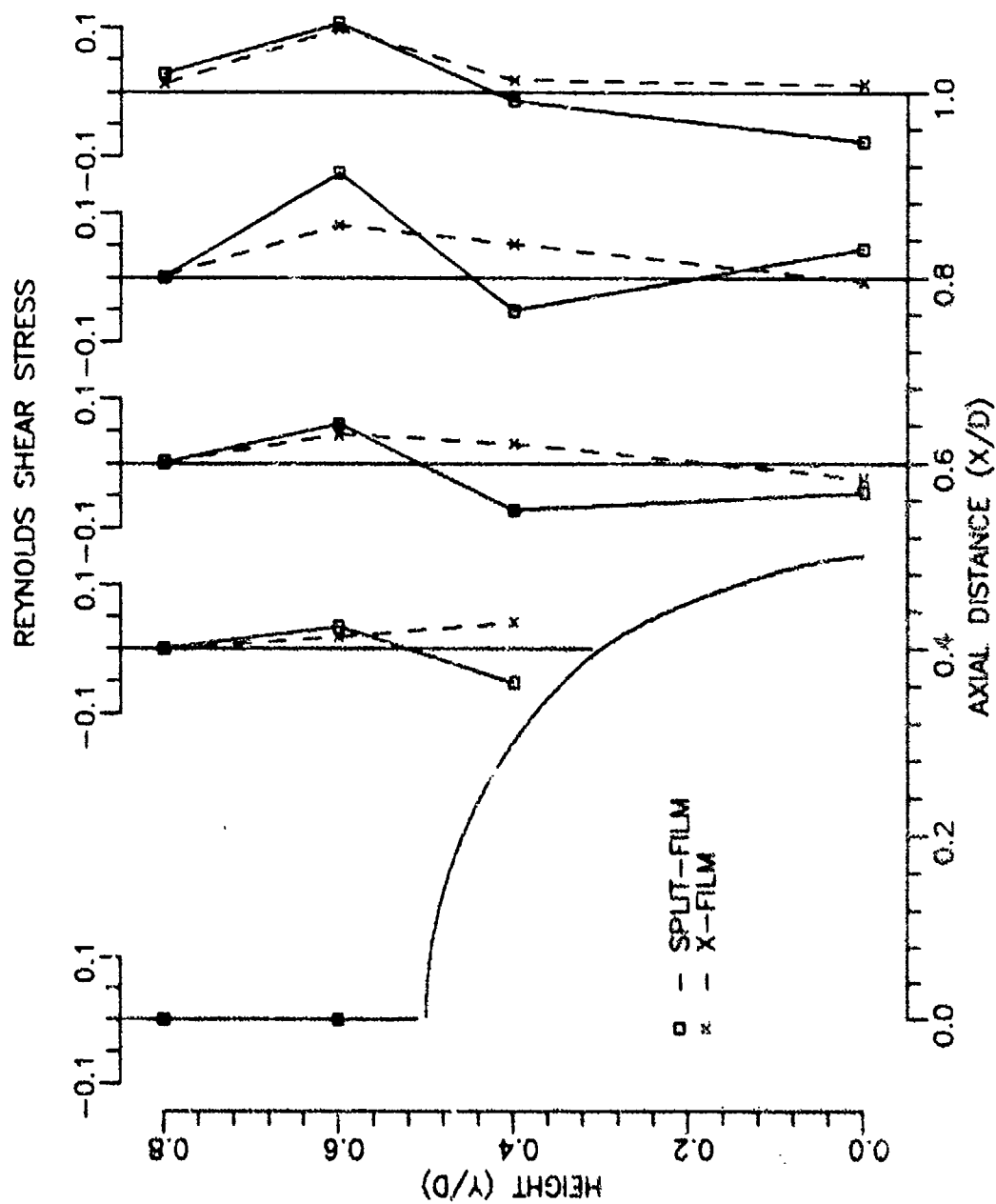


Figure 27. Reynolds Shear Stress Behind Cylinder ( $Re = 144,000$ )

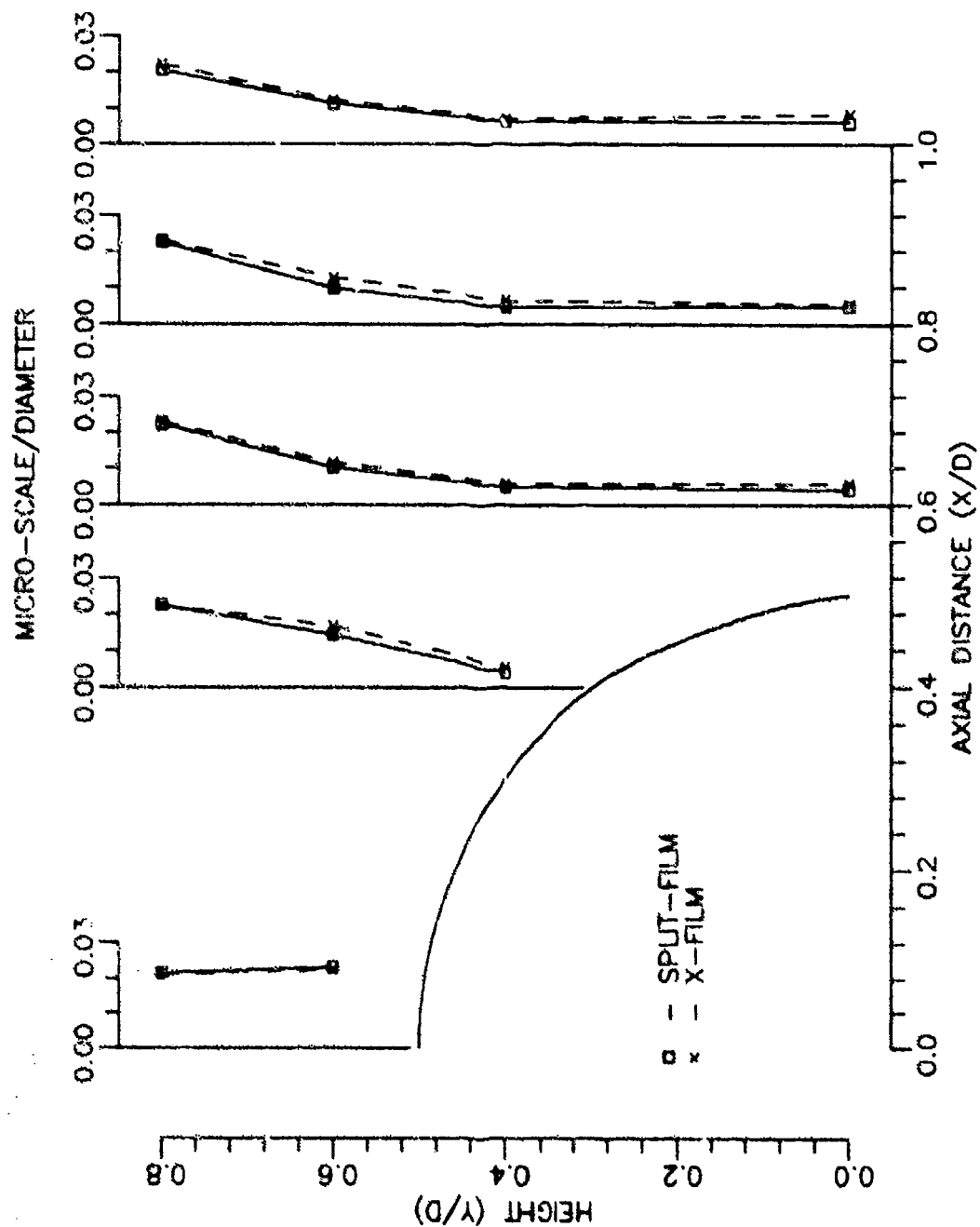


Figure 28. Turbulence Micro-scale Behind Cylinder, u-Component (Re = 144,000)

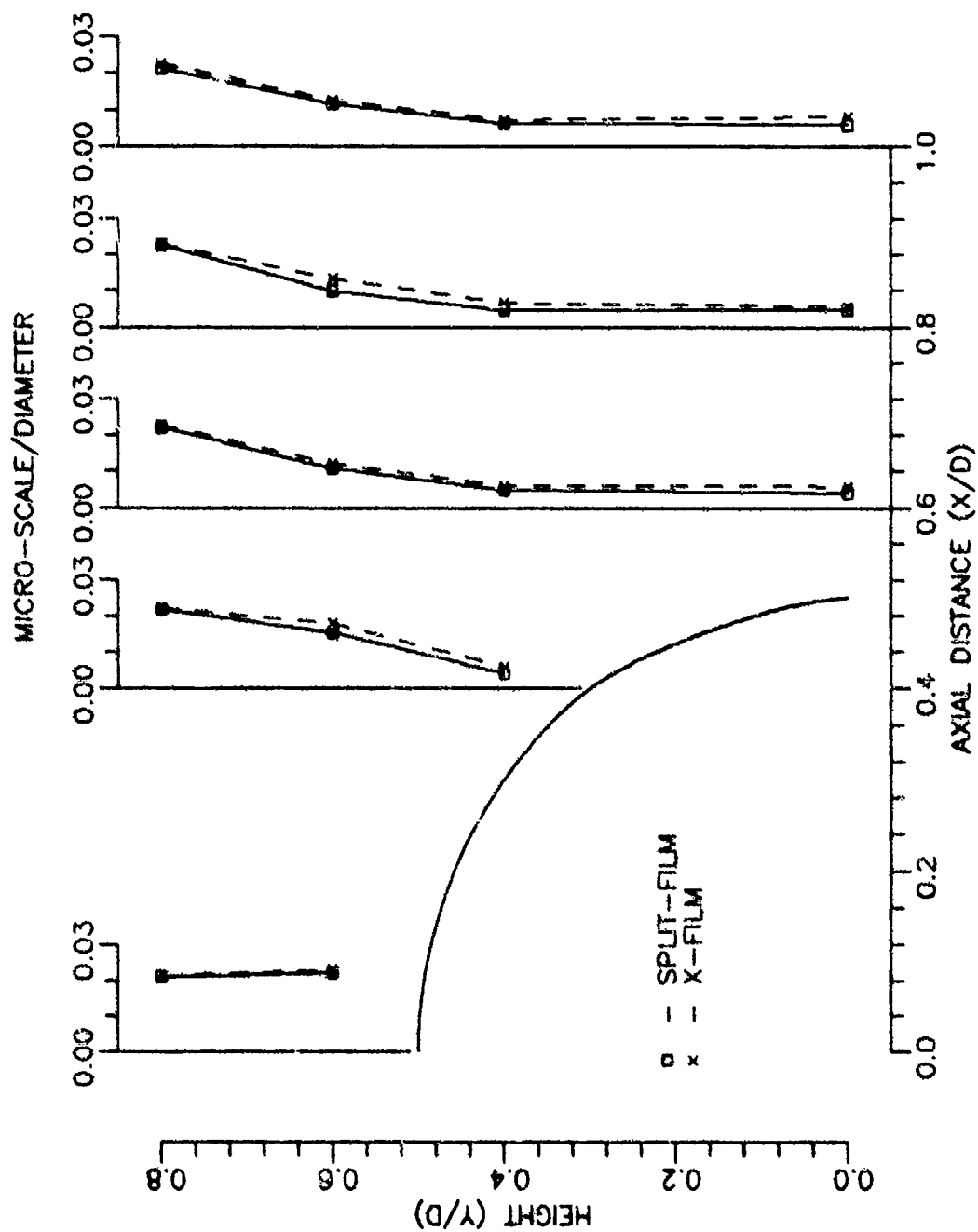


Figure 29. Turbulence Micro-scale Behind Cylinder, v-Component ( $Re = 144,000$ )

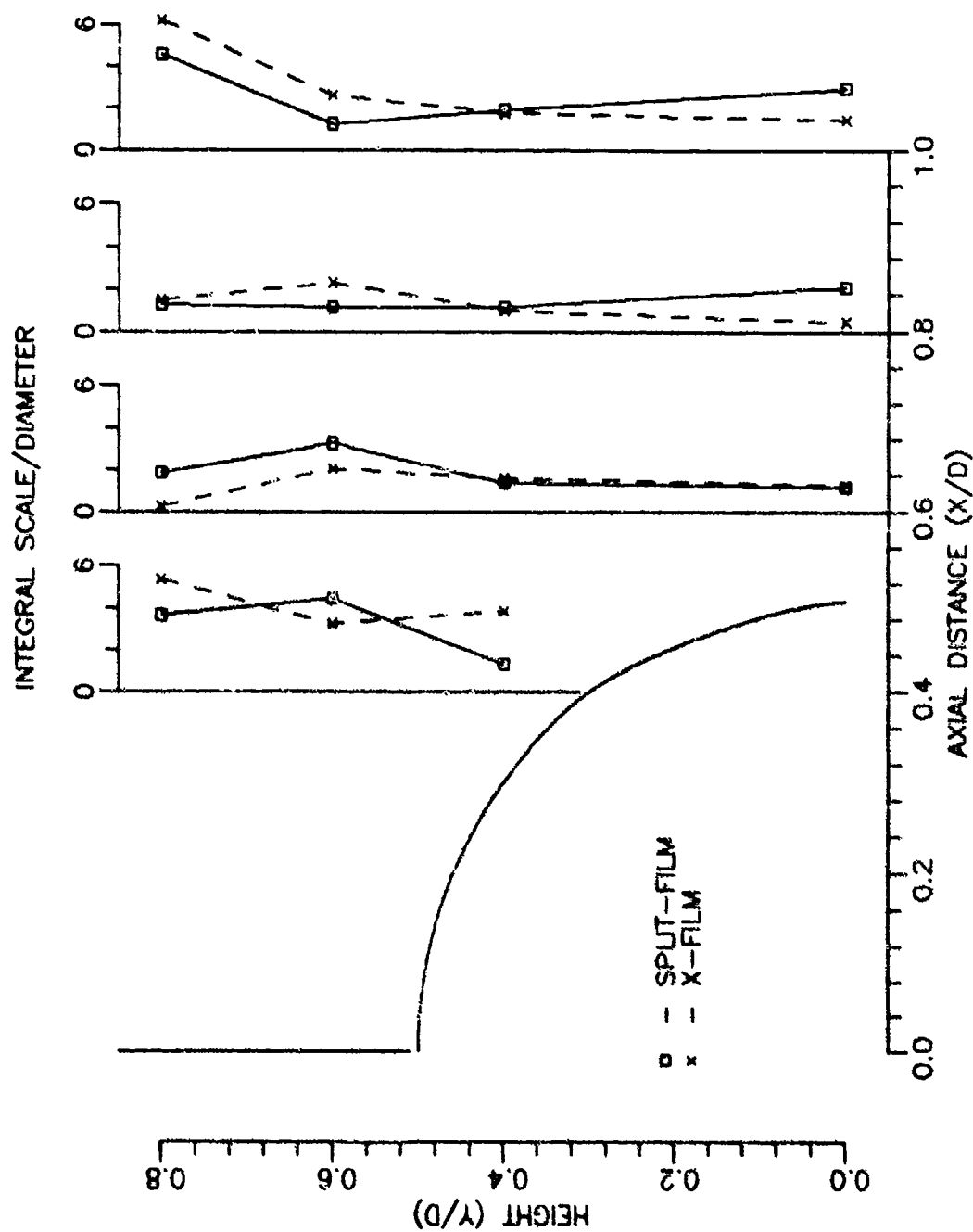


Figure 30. Turbulence Integral Scale Behind Cylinder, u-Component (Re=144,000)



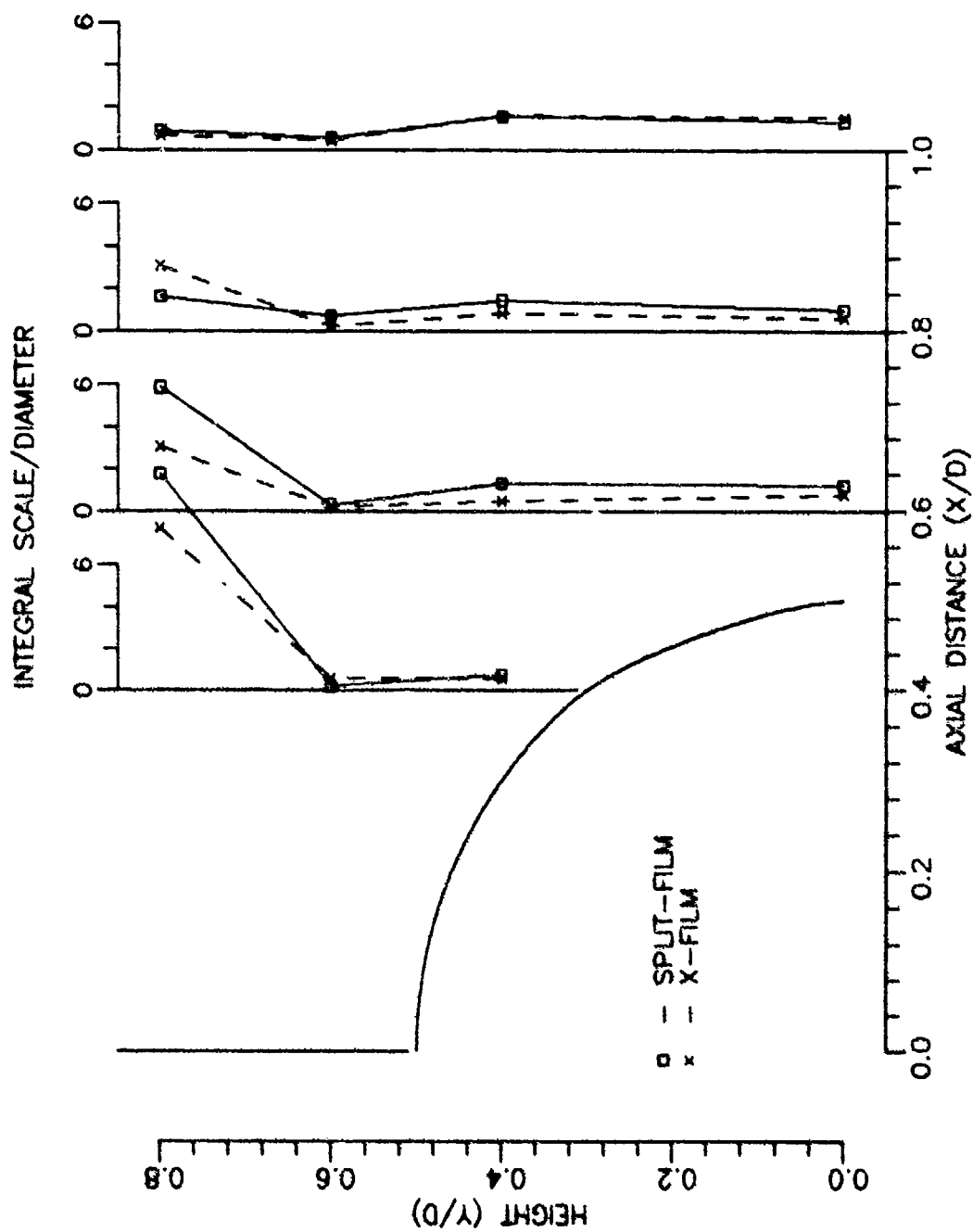


Figure 31. Turbulence Integral Scale Behind Cylinder, v-Component ( $Re=144,000$ )

## Vita

Captain Timothy E. Fisk was born on 2 August 1957 in Olean, New York. He graduated from high school in Allegany, New York, in 1975 and attended the State University of New York at Alfred where he received an Associate Degree in Engineering Science in 1977. Upon graduation, he enlisted in the USAF and worked as an Aircraft Weapons Loader at Shaw AFB, South Carolina. Concurrent with his enlistment he attended the University of South Carolina in Columbia South Carolina and later received a Bachelor of Science in Mechanical Engineering in May 1982. He separated from active duty in November 1981 and began his engineering career with Grove Manufacturing in Conway, South Carolina, where he worked as a Senior Hydraulic Systems Design Engineer. In April 1983 he entered USAF Officer Training and was commissioned in July 1983. He then served as a Program Engineer in the Armament Division Support Equipment Program Office at Eglin AFB, Florida until entering the Air Force Institute of Technology-School of Engineering in May 1987.

Permanent address: 5541 Signet Drive  
Dayton, OH 45424

# REPORT DOCUMENTATION PAGE

Form Approved  
OMB No. 0704-0188

1a. REPORT SECURITY CLASSIFICATION UNCLASSIFIED			1b. RESTRICTIVE MARKINGS		
2a. SECURITY CLASSIFICATION AUTHORITY			3. DISTRIBUTION / AVAILABILITY OF REPORT Approved for public release; distribution unlimited		
2b. DECLASSIFICATION / DOWNGRADING SCHEDULE					
4. PERFORMING ORGANIZATION REPORT NUMBER(S) AFIT/GAE/AA/88D-16			5. MONITORING ORGANIZATION REPORT NUMBER(S)		
6a. NAME OF PERFORMING ORGANIZATION School of Engineering		6b. OFFICE SYMBOL (If applicable) AFIT/ENY	7a. NAME OF MONITORING ORGANIZATION		
6c. ADDRESS (City, State, and ZIP Code) Air Force Institute of Technology Wright-Patterson AFB OH 45433-6583			7b. ADDRESS (City, State, and ZIP Code)		
8a. NAME OF FUNDING / SPONSORING ORGANIZATION		8b. OFFICE SYMBOL (If applicable)	9. PROCUREMENT INSTRUMENT IDENTIFICATION NUMBER		
8c. ADDRESS (City, State, and ZIP Code)			10. SOURCE OF FUNDING NUMBERS		
			PROGRAM ELEMENT NO.	PROJECT NO.	TASK NO.
			WORK UNIT ACCESSION NO.		
11. TITLE (Include Security Classification) COMPARISON OF SPLIT-FILM AND X-FILM MEASUREMENTS IN 2-D FLOW (UNCLASSIFIED)					
12. PERSONAL AUTHOR(S) Timothy E. Fisk, B.S., Capt, USAF					
13a. TYPE OF REPORT MS Thesis		13b. TIME COVERED FROM _____ TO _____		14. DATE OF REPORT (Year, Month, Day) 1988, November	
15. PAGE COUNT 65					
16. SUPPLEMENTARY NOTATION					
17. COSATI CODES			18. SUBJECT TERMS (Continue on reverse if necessary and identify by block number)		
FIELD	GROUP	SUB-GROUP			
U5	01		SPLIT-FILM X-FILM ANEMOMETRY		
19. ABSTRACT (Continue on reverse if necessary and identify by block number)					
<p>Thesis Advisor: LtCol Paul I. King Department of Aeronautics and Astronautics Assistant Professor of Aerospace Engineering</p>					
<p>Approved for release in accordance with AR 150-1 J. R. Rasmussen 12 Jan 1997</p>					
20. DISTRIBUTION / AVAILABILITY OF ABSTRACT <input checked="" type="checkbox"/> UNCLASSIFIED / UNLIMITED <input type="checkbox"/> SAME AS RPT <input type="checkbox"/> DTIC USERS			21. ABSTRACT SECURITY CLASSIFICATION UNCLASSIFIED		
22a. NAME OF RESPONSIBLE INDIVIDUAL LtCol Paul I. King			22b. TELEPHONE (Include Area Code) (513) 255-2362		22c. OFFICE SYMBOL AFIT/ENY

64

Abstract

The split-film sensor is composed of two independent films supported by a quartz filament. The split-film's larger diameter makes it less sensitive to high frequency fluctuations than the x-film, but is able to measure higher flow angles than the x-film. The objective of this thesis is to compare turbulence measurements of the split-film with the more established x-film over a range of turbulence levels.

The results indicate problems using the split-film in regions of low velocity combined with low turbulence (Reynolds number based on film diameter less than 380 and turbulence intensity below 1.5 percent). The split-film provided better turbulence measurements than the x-film when used in regions of high turbulence (10 to 50 percent) with velocity fluctuations greater than 45 degrees from the mean.

The split-film is not capable of detecting flow reversals, but will give the proper direction of the velocity component normal to the split. This information is helpful because the magnitude of the Reynolds shear stress in reversing flow can still be determined using the split-film, but not the direction (sign).